SCIENTIFIC REPORT

INFRARED INTERFEROMETRY, YOUNG STELLAR OBJECTS, EVOLVED STARS, ACTIVE GALACTIC NUCLEI, AND COSMIC RAYS

1 YOUNG STELLAR OBJECTS: INFRARED INTERFEROMETRY AND RADIATIVE TRANSFER MODELING OF DISKS AND OUTFLOWS

1.1 VLTI/MIDI and VLTI/AMBER infrared interferometry of the Herbig Be star MWC 147: detection of optically thick gas in the inner accretion disk

According to the current paradigm, accretion disks are an integral part of the star formation process, providing the stage where planet formation takes place. Herbig AeBe (HAeBe) stars are pre-main sequence stars of intermediate mass ($\sim 2-10\ M_{\odot}$) that show broad emission lines, rapid variability, and excess infrared and millimeter-wavelength emission. These properties suggest the presence of substantial amounts of circumstellar dust and gas around HAeBes, but the distribution of this circumstellar material is still a matter of debate. Since the spatial scales of the inner circumstellar environment (a few AU, corresponding to <0.1") were not accessible to optical and infrared imaging observations until recently, conclusions drawn on the spatial distribution of the circumstellar material were, in most cases, based entirely on the modeling of the spectral energy distribution (SED). We investigated the geometry of the inner (AU-scale) circumstellar region around the Herbig Be star MWC 147 using ESO's Very Large Telescope Interferometer (VLTI). By combining near- (NIR) and mid-infrared (MIR) spectro-interferometry of a Herbig star for the first time, our AMBER and MIDI data constrain not only the geometry of the brightness distribution, but also the radial temperature distribution in the disk. The emission from MWC 147 is clearly resolved and has a characteristic physical size of $\sim$1.3 AU at 2.2 μm and $\sim$9 AU at 11 μm. The MIR emission reveals elongation consistent with a disk structure seen under intermediate inclination.

For a detailed modeling of the interferometric data and the SED of MWC 147, we employ 2-D radiative transfer simulations. This analysis shows that models of spherical envelopes or passive, irradiated Keplerian disks (with and without puffed-up inner rims) can easily fit the SED but predict a much lower visibility than observed; the angular size predicted by such models is 2 to 4 times larger than the size derived from the interferometric data, so these models can clearly be ruled out. Models of a Keplerian disk with optically thick gas emission from an active gaseous disk (inside the dust sublimation zone), however, yield a good fit of the SED and simultaneously reproduce the absolute level and the spectral dependence of the NIR and MIR visibilities (Fig. 1). We conclude that the NIR continuum emission from MWC 147 is dominated by accretion luminosity emerging from an optically thick inner gaseous disk, while the MIR emission also contains contributions from the outer, irradiated dust disk. (Kraus et al. 2007, submitted)

1.2 VLTI/MIDI mid-infrared interferometry of the compact dusty disk around the Herbig Ae star HR 5999

We carried out mid-infrared long-baseline interferometry to resolve the circumstellar material around the Herbig Ae star HR 5999, to provide the first direct measurement of its angular size, and to derive constraints on the spatial distribution of the circumstellar dust. VLTI/MIDI was used to obtain a set of ten spectrally dispersed (8$-$13 μm) interferometric measurements of HR 5999 at different projected baseline lengths and position angles. To derive constraints on the geometrical distribution of the dust, we compared our interferometric measurements to 2-D, frequency-dependent radiative transfer models of circumstellar disks and envelopes. The derived visibility values show that the mid-infrared emission from

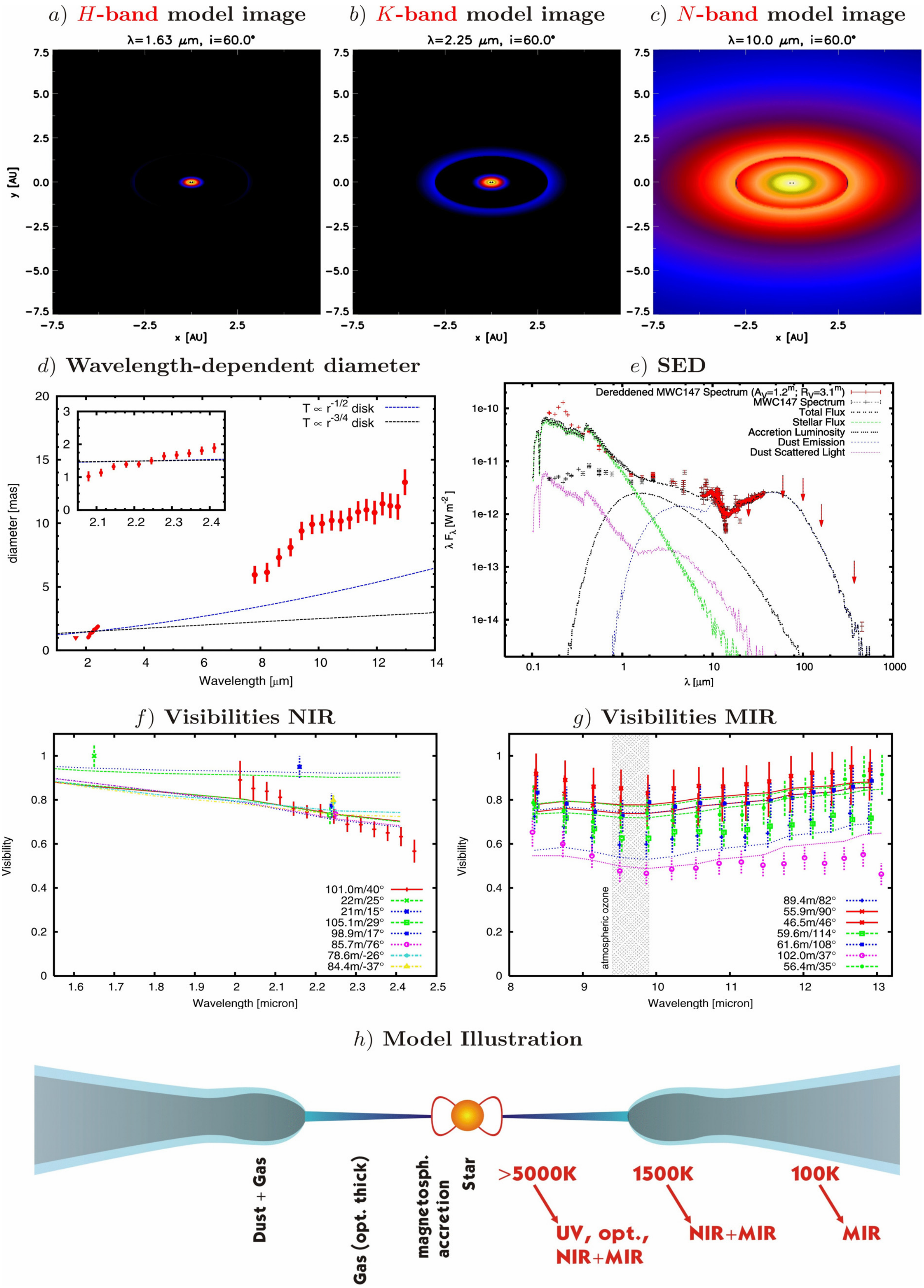

Figure 1 Comparing the wavelength-dependence of the measured characteristic size of MWC 147 over the H-, K- and N-bands with temperature-power-law disk models, we find that these routinely applied models cannot describe our data (see diameter discrepancy between observation and model in panel d). Therefore, we performed a detailed study using 2-D radiative transfer models of Keplerian disk geometries and computed the brightness distribution (a to c), the SED (e), and the visibilities (f & g). Comparing the model visibilities to our spectro-interferometric data, we find a best-fit model (χ^2_r=1.26) which includes not only an outer dust disk, but also thermal emission from optically thick gas inside the dust sublimation radius (see panel h for a model illustration).

HR 5999 is clearly resolved. The characteristic size of the emission region ranges between ~5−15 milliarcseconds (Gaussian FWHM), corresponding to remarkably small physical sizes of ~1−3 AU. For disk models with radial power-law density distributions, the relatively weak but very extended emission from outer disk regions (>3 AU) leads to model visibilities that are significantly lower than the observed visibilities, making these models inconsistent with the MIDI data. On the other hand, disk models in which the density is truncated at outer radii of ~2−3 AU provide good agreement with the data. A satisfactory fit to the observed MIDI visibilities of HR 5999 is found with a model of a geometrically thin disk that is truncated at 2.6 AU and seen under an inclination angle of 58° (i.e. closer to an edge-on view than to a face-on view). Neither models of a geometrically thin disk seen nearly edge-on nor models of spherical dust shells can achieve agreement between the observed and predicted visibilities. We speculate that the compactness of the disk is due to truncation by a close binary companion. (see Preibisch et al. 2006)

1.3 VLTI/AMBER interferometry of the disk-wind region of the Herbig star HD 104237

Besides their characteristic infrared excess continuum emission, Herbig AeBe stars are known to show line emission, mainly from hydrogen. Although this has been known for decades, the spatial origin of the line emission is still strongly debated. For instance, it has been suggested that the Br γ line at 2.16 μm traces gas which is just accreted onto the star through magnetospheric accretion columns (Fig. 2a), while others associate the line with stellar winds (Fig. 2b) or emission from outflows launched from a circumstellar disk (Fig. 2c). Using the unique medium spectral resolution mode of VLTI/AMBER (spectral resolution=1500), we investigate the origin of the Br γ emission of the Herbig Ae star HD 104237. With a baseline of 35 m, we spatially resolve the emission in both the Br γ line and the adjacent continuum. We assume that the K-band continuum excess originates in a puffed-up inner rim zone of the circumstellar disk and discuss the likely origin of the Br γ emission. The visibility does not vary between the continuum and the Br γ line (right panel of Fig. 2), even though the line is strongly detected in the spectrum, with a peak intensity 35% above the continuum. This demonstrates that the line- and continuum-emitting regions have similar spatial scales. We conclude that the line emission most likely arises from a region 0.2–0.5 AU from the star with a spatial extent similar to that of the near infrared continuum emission region; i.e., very close to the inner rim location. This result suggests that the gas emission does not originate close to the star (as expected in the magnetospheric accretion or stellar wind scenario), but likely from a wind which is launched from the disk and then collimated into the jet associated with this object (Grady et al. 2004, ApJ 608, 809). (see Tatulli et al. 2007)

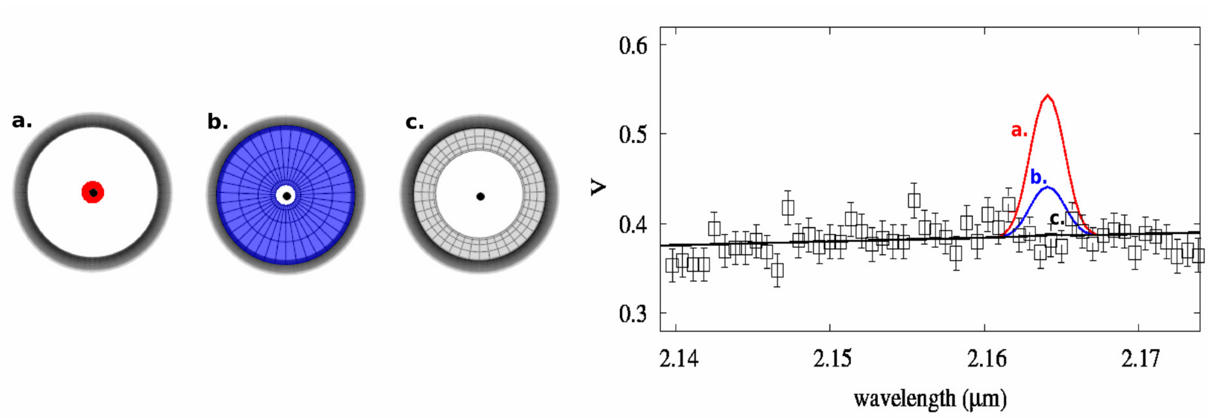

Figure 2 *Comparison of different models of the wind emission origin of HD 104237: In scenario (a), the Br γ emission (shown in red) originates in a magnetospheric accretion region, which is much more compact than the dust inner rim (shaded gray). Alternatively, the Br γ emission could emerge from a gaseous disk located between the dust disk and the star (b). Since both of these scenarios predict a rise in the visibility within the Brγ emission line, which is not observed in our AMBER data (as shown in the right panel, open squares), we favor a disk wind scenario where most of the Br γ emission originates close to the inner rim of the dust disk (c).*

1.4 Bispectrum speckle interferometry and IOTA 3-telescope interferometry of the Orion Trapezium Star θ^1 Orionis C: Preliminary dynamical orbit solution and first infrared aperture-synthesis image of a young binary

Located in the Orion Trapezium cluster, θ^1 Ori C is one of the youngest and nearest high-mass stars (O5-O7) known. Besides its unique properties as a magnetic rotator, the system is also known to be a close binary. Since the discovery of the companion by our group in 1997 (Weigelt et al. 1999, A&A 347, L15), we have traced the orbital motion of the system with the aim of determining the orbit and dynamical mass of the system. In addition to a characterization of the individual components, ultimately, this will yield new constraints for stellar evolution models in the high-mass regime. Furthermore, a dynamical parallax can be derived from the orbit, providing an independent estimate for the distance of the Trapezium cluster.

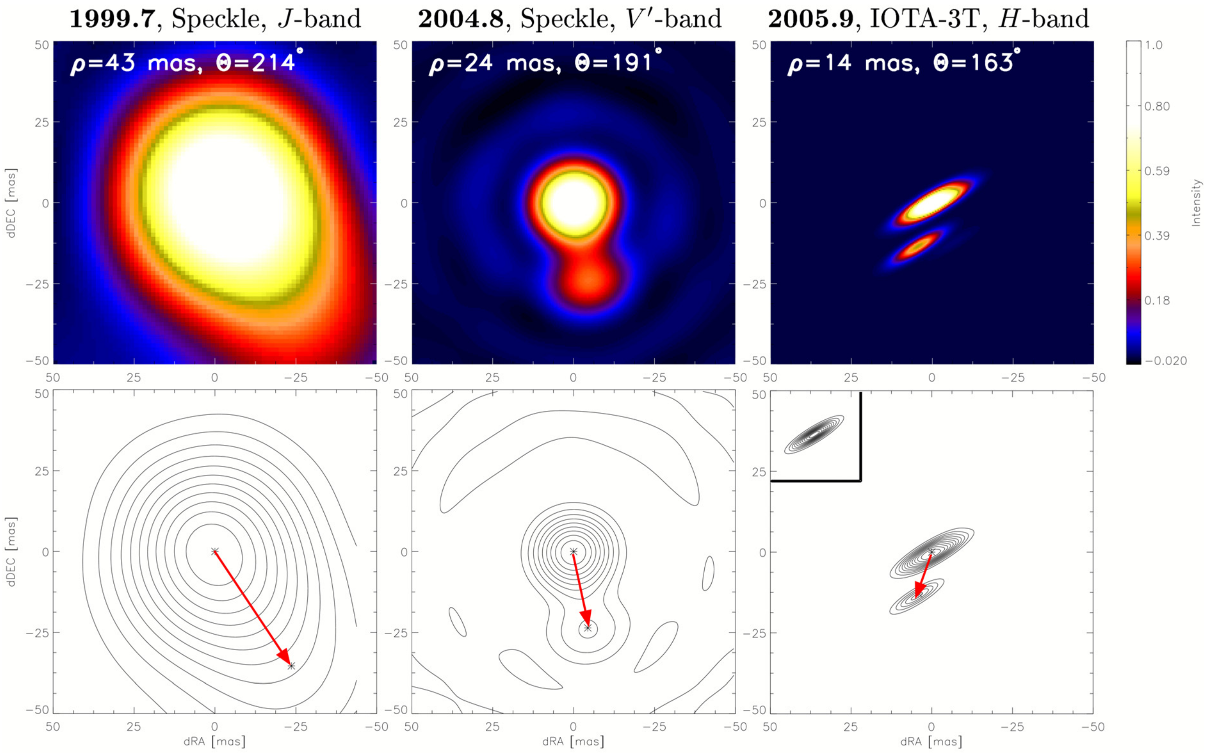

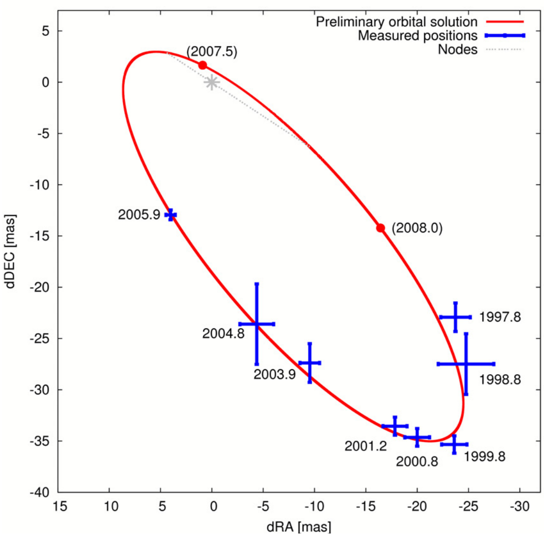

Figure 3 *Top: After following the orbital motion of the θ^1 Ori C components over 7 years using bispectrum speckle interferometry at near-infrared and visual wavelengths (left and middle), we obtained the first long-baseline interferometry (right) of the system in 2005 with the IOTA 3-telescope interferometer, which provides baselines up to 38 m (top panels: ρ=separation, θ=position angle). Bottom: Our best-fit preliminary orbital solution for θ^1 Ori C (red line) predicts a highly eccentric orbit with periastron passage already in 2007.*

Using new multi-epoch visual and near-infrared bispectrum speckle interferometric observations obtained at the BTA 6 m telescope and IOTA near-infrared long-baseline interferometry, we traced the orbital motion of the θ^1 Ori C components from 1997.8 to 2005.9 (Fig. 3), covering a significant arc of the orbit. Besides fitting the relative position and the flux ratio, we applied aperture-synthesis techniques to our IOTA data to reconstruct a model-independent image of the θ^1 Ori C binary system (Fig. 3, top right). This is the first image of a young binary obtained using the IR long-baseline interferometry technique. Taking the measured flux ratio and the derived location in the HR-diagram into account, we find good agreement for all observables, assuming a spectral type of O5.5 for θ^1 Ori C1 ($M=34.0\ M_\odot$, $T_{eff}=39900$ K) and O9.5 for C2 ($M=15.5\ M_\odot$, $T_{eff}=31900$ K).

Our preliminary orbital solution for the system suggests a highly eccentric ($e\approx0.91$) and short-period ($P\approx10.9$ yrs) orbit. We find indications that the companion C2 is massive itself, which makes it likely that its contribution to the intense UV radiation field of the Trapezium cluster is not negligible. Furthermore, the high eccentricity of the preliminary orbit solution predicts a very small physical separation during periastron passage (~1.5 AU, passage around 2007/2008), which might lead to strong wind-wind interaction between the two O stars. (see Kraus et al. 2007)

1.5 Bispectrum speckle interferometry of the high-mass protostar NGC 7538 IRS1: Signatures of outflow precession

NGC 7538 IRS1 is a high-mass (30 $M_\odot$) protostar with a CO outflow, an associated ultra-compact HII region (UCHII), and an enigmatic linear methanol maser structure which might trace a Keplerian-rotating circumstellar disk (Pestalozzi et al. 2004, ApJ 603, L113). Surprisingly, the directions of the various associated axes are misaligned (see Fig. 4, top left). We investigate the near-infrared morphology of the source to clarify the relationship between the various axes. K'-band bispectrum speckle interferometry was performed at two 6-meter-class telescopes — the BTA 6 m telescope and the 6.5 m MMT. Complementary IRAC images from the Spitzer Space Telescope Archive were used to relate the structures detected with the outflow on larger scales. High-dynamic-range images (see Fig. 4, top right) show a clumpy, fan-shaped outflow structure in which we detect 18 stars and several blobs of diffuse emission.

The misalignment of various outflow axes of IRS1 is interpreted in the context of a disk precession model, using an analytic precession model as well as numerical hydrodynamic simulations of the molecular emission (Fig. 4, bottom left). The precession period is ~280 years and its half opening angle is ~40°. A possible triggering mechanism is the non-coplanar tidal interaction of a close (undiscovered) companion with the circumbinary protostellar disk. (see Kraus et al. 2006)

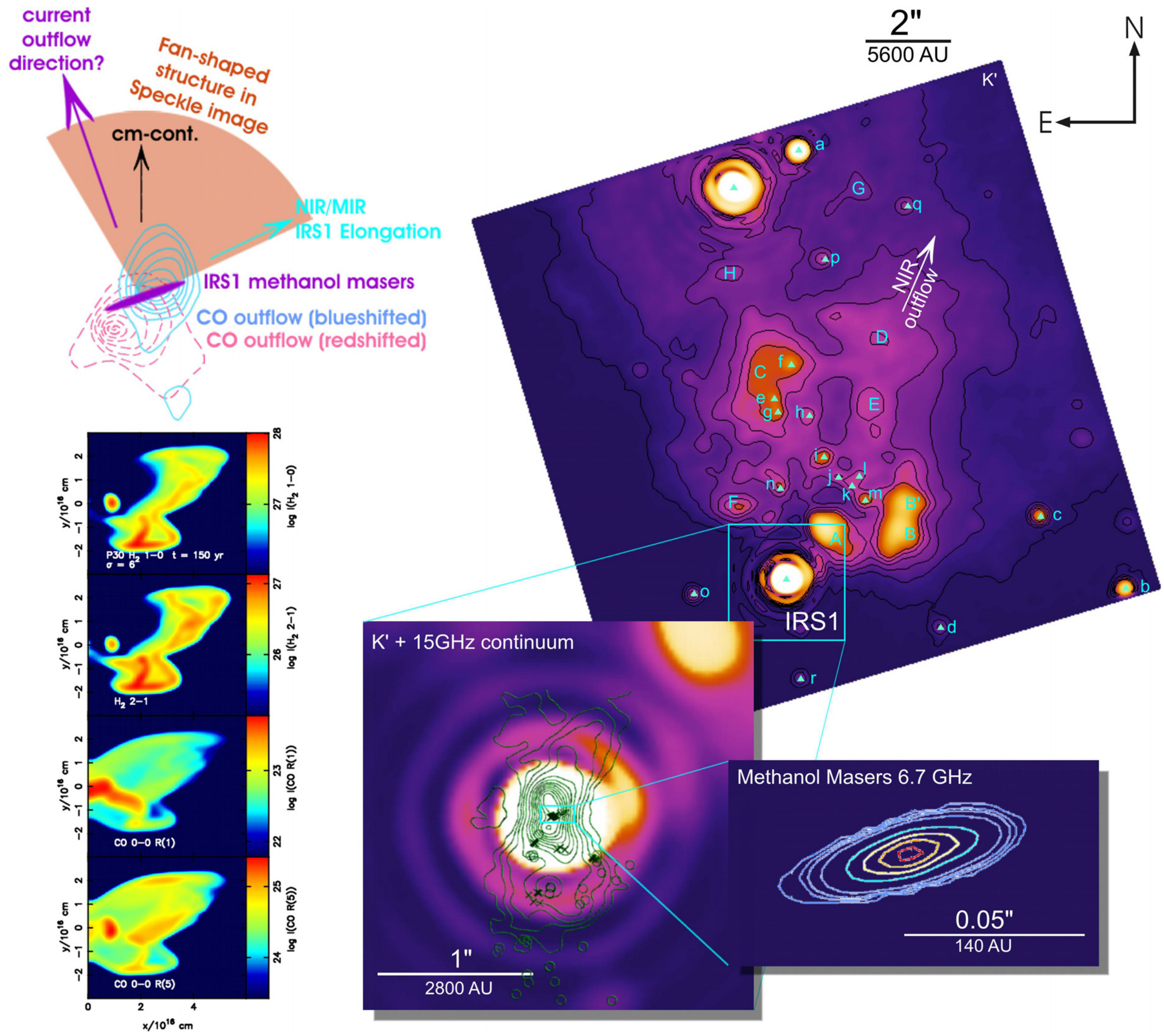

Figure 4 *Top left: Comparing the orientation of the NGC 7538 IRS1 putative methanol maser disk with the direction of various outflow tracers, such as CO and H_2, suggests that their axes are misaligned. Right: Our bispectrum speckle images (K band) allow us to compare the morphology of the clumpy NIR outflow structures around IRS1 with the position and orientation of the UCHII region (bottom middle; contour image) and the putative maser disk (bottom right). Bottom left: Using molecular hydrodynamics simulations, we model the propagation and CO and H_2 line emission of a precessing outflow, finding structures similar to those observed in our NGC 7538 IRS1 speckle image.*

1.6 Numerical simulations of protostellar jets: Determining the velocity dependence of the internal structure

Jets of gas released from young stars excavate cavities and drive bipolar outflows. We performed axisymmetric hydrodynamic simulations to determine if the observed collimated structures could be related to the speed of such jets (Fig. 5). We consider the propagation of supersonic, over-dense jets with radiative cooling and chemistry and build on previous studies by injecting molecular and atomic jets with a wide range of speeds, between 50 and 300 km s^{-1}, into both molecular and atomic media. We show that the high collimation of outflows driven by molecular jets holds for all jet speeds (Fig. 5). At higher speeds, we find that the jet Mach number is the critical parameter which determines the shape of the cavity. However, at low speeds, the jet material is the key factor, with atomic jets producing much wider cavities while molecular jets produce narrow, cool molecular sheaths. A Mach disk is associated with the leading edge of the atomic simulations, while oblique shocks which refocus the jet are found in molecular flows. We conclude that the properties of bipolar outflows possess signatures related to the jet speed, but they may be more dependent on other factors. (see Moraghan et al. 2006)

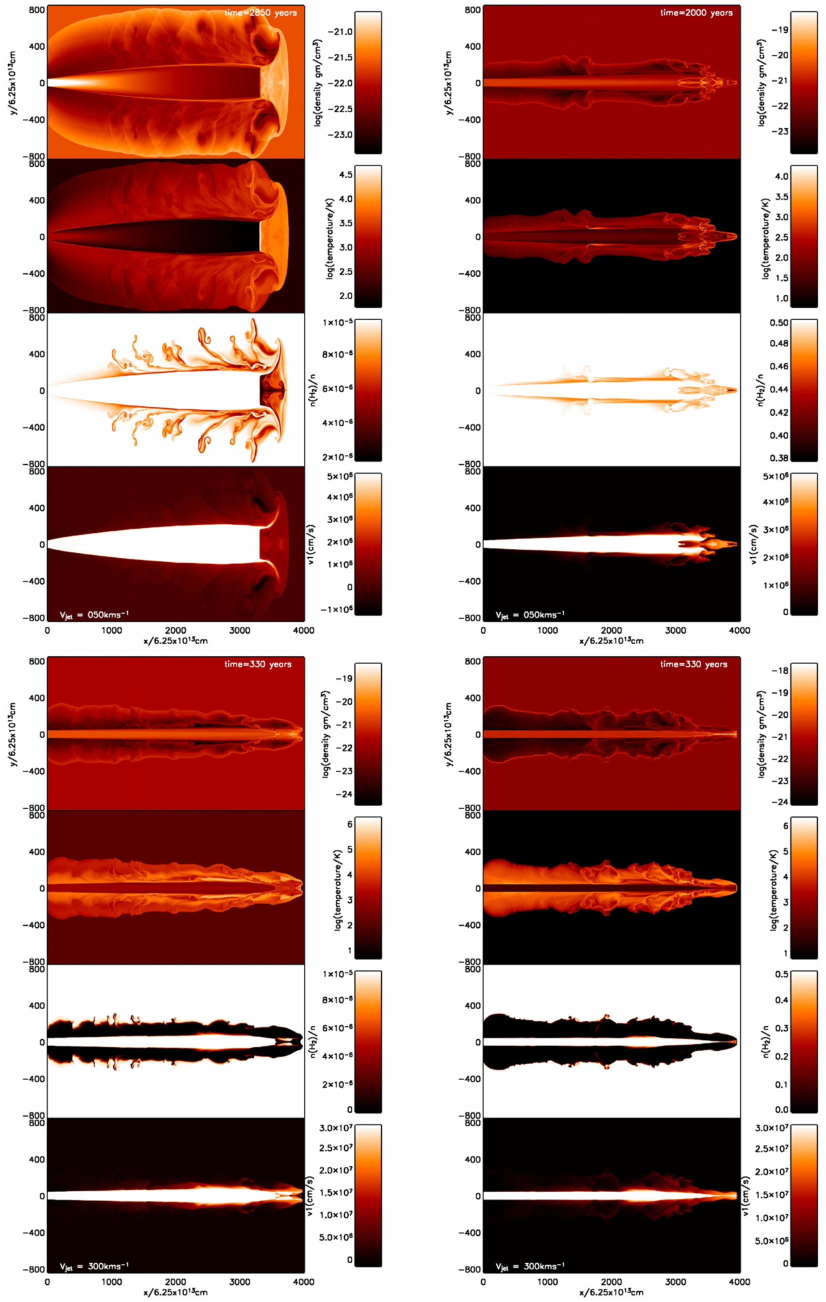

***Figure 5** Numerical simulations of protostellar jets: Cross-sectional distributions of physical parameters. The top 8 panels show a jet with a speed of 50 km s^{-1}, while for the bottom 2x4 panels, the jet speed is 300 km s^{-1}. In each of these pairs, the left column of figures represents an atomic jet propagating into an atomic ambient medium, while the right column represents a molecular jet propagating into a molecular ambient medium. Each column shows distributions of density, temperature, molecular fraction, and axial velocity (from top to bottom).*

1.7 X-ray activity of T Tauri stars in Taurus-Auriga: the relation between X-ray luminosity, rotation, and accretion

The XMM-Newton Extended Survey of the Taurus Molecular Cloud (XEST) consists of 28 deep X-ray observations of regions of the Taurus-Auriga complex that are most densely populated by T Tauri stars. These data have been used to perform the most sensitive survey of X-ray emission (0.3-10 keV) from young stars in Taurus-Auriga to date. One important part of this project was to investigate the dependences of X-ray activity measures on the rotation period and make a detailed comparison of the X-ray properties of accreting and non-accreting stars. In order to find clues towards the origin of the strong X-ray emission from T Tauri stars, we determined the convective turnover timescales of the individual stars and computed the corresponding Rossby numbers (i.e., the ratio of the rotation period and the convective turnover timescale). A detailed comparison of the relation between the fractional X-ray luminosities (i.e., the ratio of X-ray and bolometric luminosity) of the T Tauri stars and their Rossby numbers was performed with the well-known relation between these quantities shown by late-type main-sequence stars (Fig. 6). It was found that non-accreting T Tauri stars show X-ray activity entirely consistent with the saturated activity of fast-rotating, late-type main-sequence stars.

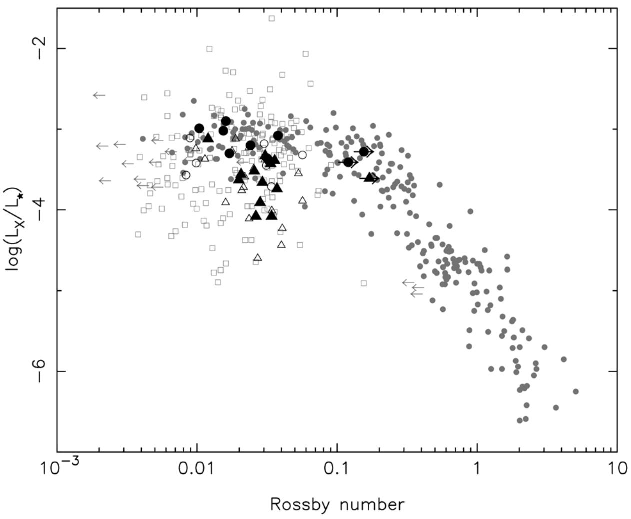

Figure 6 *Ratio of X-ray and stellar luminosities as a function of the Rossby number. The filled grey circles show data for late-type main sequence stars (Pizzolato et al. 2003), the grey squares data for T Tauri stars in the Orion Nebula Cluster (Preibisch et al. 2005), and the black circles/triangles show non-accreting/accreting T Tauri stars in Taurus-Auriga.*

Accreting T Tauri stars show lower X-ray activity, independent of rotation. Accretors have lower absolute as well as fractional X-ray luminosities than non-accretors, independent of other stellar parameters such as mass, luminosity, and rotation period. The results of this study point toward some effect of the coupling of the stellar surface and atmosphere to circumstellar material, rather than a reduced dynamo efficiency, as the cause of the lower X-ray output of accreting T Tauri stars. (see Briggs et al. 2007)

2 STARS IN LATE EVOLUTIONARY STAGES

2.1 First infrared spectro-interferometry of the Luminous Blue Variable η Car with spectral resolutions of 1500 & 12000: resolution of the optically thick wind zone

The enigmatic object η Car is one of the most luminous and most massive ($M{\sim}100\ M_\odot$) unstable Luminous Blue Variables suffering from an extremely high mass loss. η Car is located at a distance of approximately 2300 pc and is surrounded by the expanding bipolar Homunculus nebula ejected during the Great Eruption in 1843. We carried out the first spectro-interferometric observations of η Car. The observations were performed with three 8.2 m telescopes of the VLTI (baselines in the range of 42 to 89 m) and the VLTI/AMBER instrument. The aim of this work is to study η Car's stellar wind region in the continuum as well as in emission lines with a high spatial resolution of 5 mas (11 AU) and high spectral resolution. The raw data are spectrally dispersed interferograms obtained with spectral resolutions of 1500 (MR-K mode) and 12000 (HR-K mode). The MR-K observations were performed in the wavelength range around both the He I 2.059 μm and the Brackett γ 2.166 μm emission lines, the HR-K observations only in the Brγ line region.

The spectrally dispersed AMBER interferograms allow the investigation of the wavelength dependence of the visibility, differential phase, and closure phase of η Car. If we fit Hillier et al. (2001, ApJ 553, 837) models to the observed AMBER visibilities, we obtain 50% encircled-energy diameters of 4.2, 6.5, and 9.6 mas in the 2.17 μm continuum, the HeI, and the Brγ emission lines, respectively. In the continuum near the Brγ line, an elongation along a position angle of 120° was found. In Fig. 7, we compare the measured visibilities with predictions of the radiative transfer model of Hillier et al. (2001), finding good agreement. For the interpretation of the non-zero differential and closure phases measured within the Brγ line, we developed a geometric model of an inclined, latitude-dependent wind zone (see Fig. 7, bottom left). Our observations support theoretical models of anisotropic winds from fast-rotating, luminous hot stars with enhanced high-velocity mass loss near the polar regions. (see Weigelt et al. 2007)

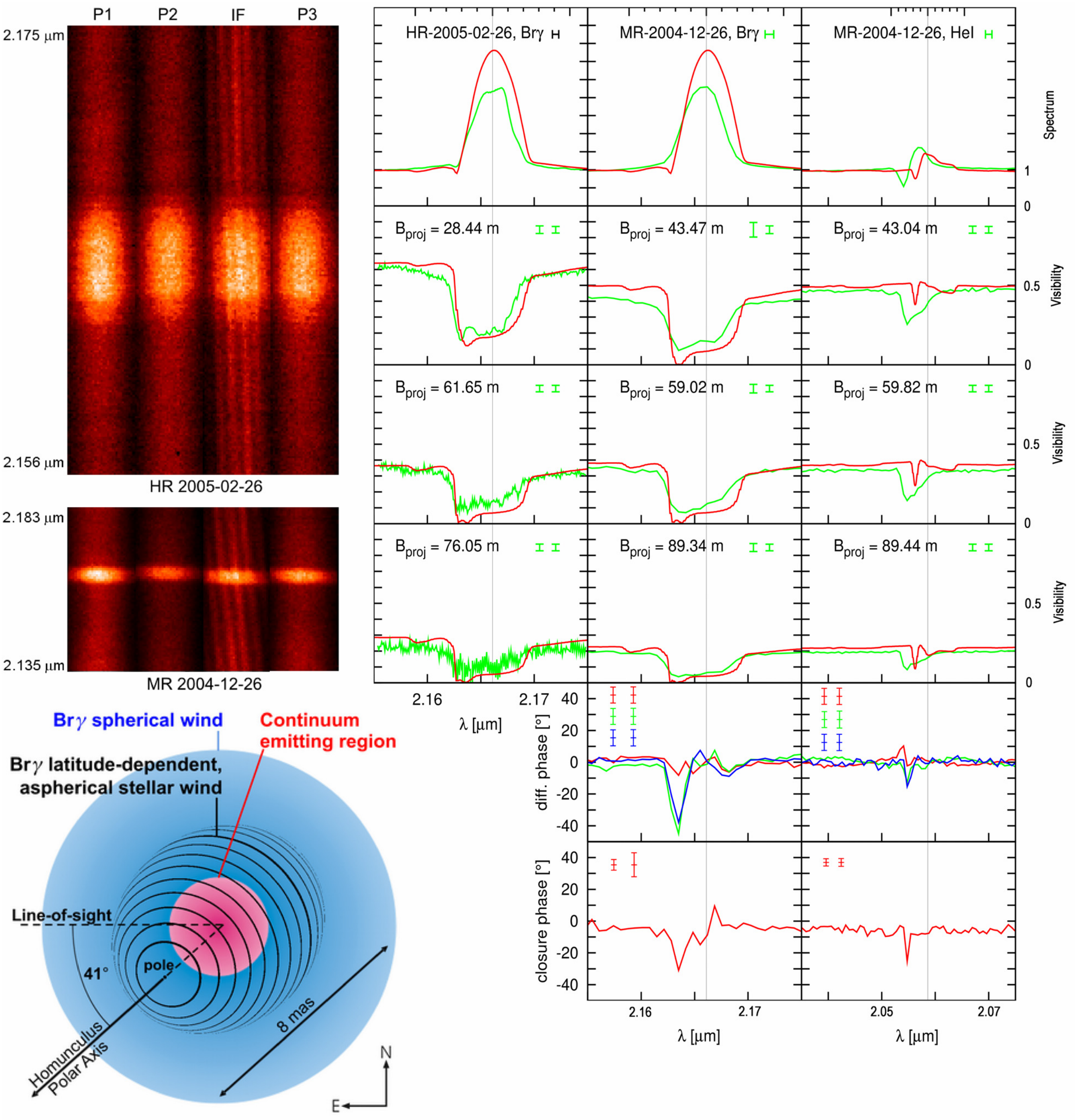

Figure 7 *Top left: Spectrally dispersed VLTI/AMBER Michelson interferogram of η Car. The panel shows the spectrally dispersed fringe signal (IF) as well as the photometric calibration signals from the three telescopes (P1-P3) in the high (top; R=12000) and medium (bottom; R=1500) spectral resolution mode. The bright regions are the Doppler-broadened Brγ emission line. Right: Comparison of the AMBER high (left column) and medium (middle and right columns) spectral resolution measurements of η Car (green lines; top row: spectra; second to fourth row: visibilities) with the gas radiative transfer model of Hillier et al. (2001, ApJ 553, 837) (red lines in the 4 uppermost panels). As the figure shows, we find good agreement between the AMBER data and the model predictions for the continuum visibilities as well as the shape and depth of the visibility inside the Brγ line. In the case of the HeI line, the wavelength dependence of the model visibility inside the line differs considerably from the AMBER measurements, indicating a different physical process involved in the line formation (emission from the wind-wind interaction zone of the binary). The two bottom rows show the differential and closure phases obtained from the two AMBER medium spectral resolution measurements. The figure at the bottom left shows the 3 components of our model, which is able to explain all observed spectra, visibilities, differential phases, and closure phases (pole=south pole of the latitude-dependent aspherical Brγ wind zone).*

2.2 VLTI/AMBER near-infrared interferometry of the nearest colliding-wind WR+O binary γ^2 Vel

We carried out VLTI/AMBER observations of the Wolf-Rayet WR+O star binary γ^2 Velorum at orbital phase 0.32 using the UT2, UT3, and UT4 8.2 m VLT telescopes with baselines ranging from 46 to 85 m. The observations provide spectrally dispersed visibilities as well as differential and closure phases with a spectral resolution of R=1500 in the K band between 1.95 and 2.17 μm. Using synthetic WR- and O-star spectra, we showed that the VLTI/AMBER data (visibilities, spectra, and closure phases) primarily measure the contributions of the individual components from the WR+O binary system. However, the ~5% residuals between model and observations suggest the presence of an additional continuum component originating from free-free emission associated with the wind-wind collision zone between the binary components. Using a geometrical double star model and spectroscopic models for the O and WR stars, we determined a binary separation of 3.62 (+0.11, -0.30) mas, a position angle of 73° (+9, -11) degree, and a distance of 368 (+38, -13) pc. (see Millour et al. 2007)

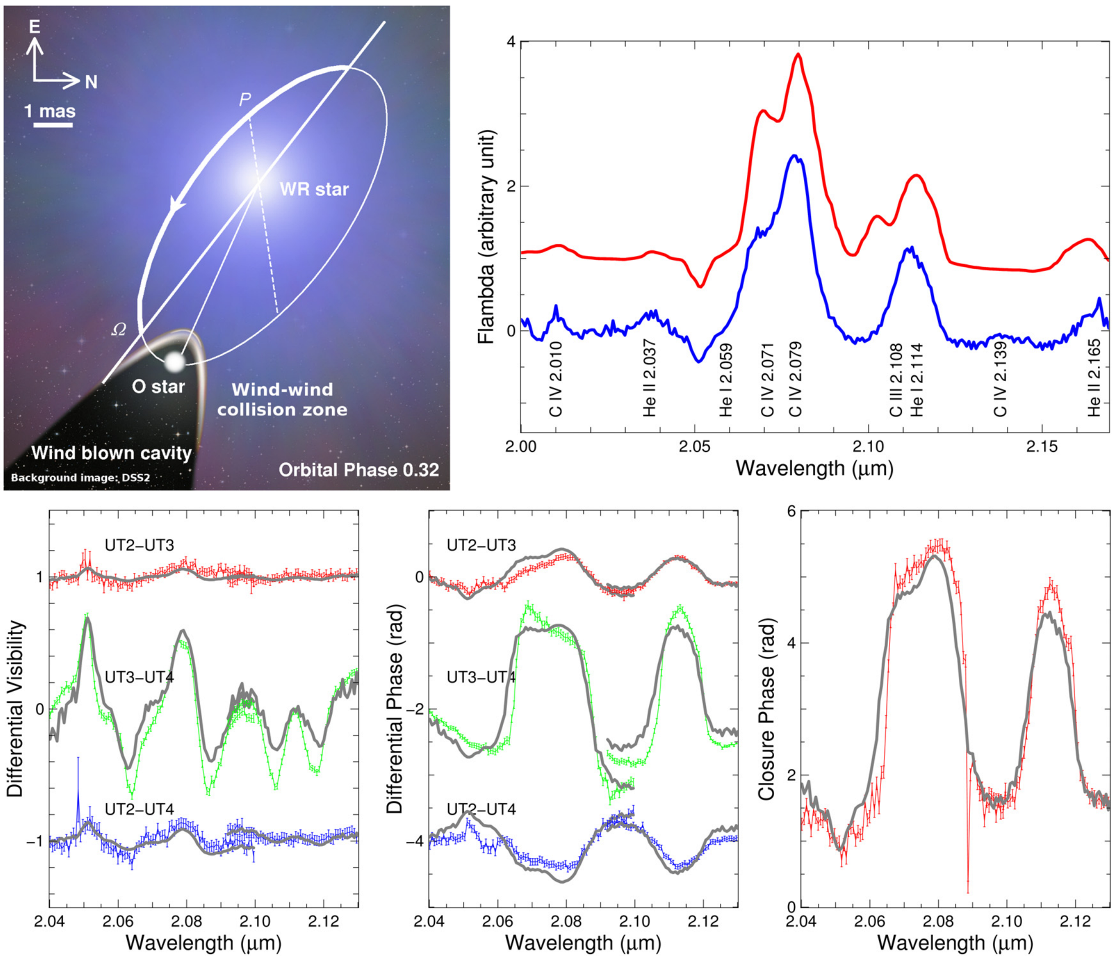

__Figure 8__ Top left: Artist's view of the binary orbit of γ^2 Vel and the colliding wind zone caused by the stellar winds from the WR and O star. Top right: Comparison between a model spectrum of the WR star (red line) and the WR spectrum derived from the observed AMBER spectrum by subtracting a synthetic O-star spectrum (blue line, down-shifted for clarity). Bottom from left to right: Differential visibilities, differential phases, and closure phases of γ^2 Vel obtained with VLTI/AMBER (spectral resolution R=1500). For the sake of clarity, vertical offsets were introduced to separate the data corresponding to different baselines (red, green, and blue lines) in the two left panels. The gray lines correspond to our best-fit model using a geometrical model of a double star, a synthetic O-star spectrum, and the spectrum of the WR-star spectrum derived fom the observations (top-right panel; blue curve).

2.3 VLTI/AMBER interferometry of the recurrent Nova RS Oph 5.5 days after outburst

We carried out spectrally dispersed interferometric VLTI/AMBER observations of the recurrent nova RS Oph only five days after the discovery of its recent outburst on 2006 Feb 12. Using three baselines ranging from 44 to 86 m and a spectral resolution of 1500, we measured the extension of the milliarcsecond-scale emission in the K band continuum, and within the Br γ and He I 2.06 μm lines. These measurements allow us to get an insight into the kinematics of the line-forming regions. The visibilities in the continuum and in the line cores (which show lower values compared to the nearby continuum, in agreement with extended line-forming regions; Fig. 9) were interpreted by fitting simple geometric models consisting of uniform and Gaussian ellipses. The ellipse models for the continuum and for the line cores are highly flattened (b/a∼0.6) and have the same major axis position angle (PA∼140°).

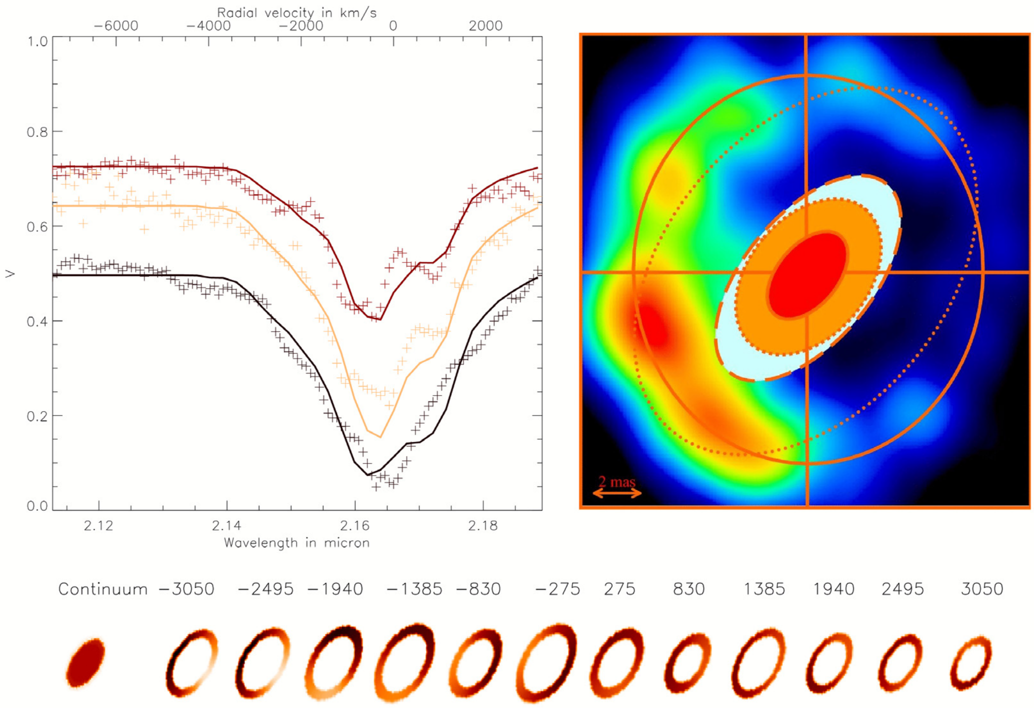

Figure 9 *Top left: Fit of the AMBER visibility measurements (crosses) of RS Oph in the Br γ line with the skewed rings models (solid line). Different colors indicate different baselines. Bottom: The model consists of a uniform ellipse for the continuum (shown only on the left) plus a 'skewed ring' that accounts for both the observed dispersed visibilities and differential phases (labels give velocity in km s^{-1}). The images at each velocity channel are normalized and do not reflect the relative fluxes in the different velocity channels. Only 12 out of 35 spectral channels covering the Br γ line region are shown. Top right: Sketch of the extension of the near-IR ellipses compared with the radio structure observed at t=13.8 d (large ring-like, false-color intensity distribution, O'Brien et al. 2006, Nat. 442, 279). The continuum and the cores of the Br γ and He I lines are delimited by the red, orange, and light-blue ellipses, respectively. The large dotted ellipse delimits the Br γ ellipse scaled to t=13.8 d.*

Their typical Gaussian extensions are 3.1×1.9 mas, 4.9×2.9 mas, and 6.3×3.6 mas for the continuum, Br γ, and He I 2.06 μm lines, respectively. The visibilities and differential phases in each of the 35 spectral channels of the Brγ line were interpreted using skewed ring models aiming to reconstruct the extension and kinematics of the line-forming region. Two radial velocity fields are apparent: a slowly expanding ring-like structure (v_{rad}≤1800 km s^{-1}) and a fast structure extended in the E-W direction (v_{rad}∼2500−3000 km s^{-1}), a direction that coincides with the jet-like structure seen at radio wavelengths. Our results confirm the basic picture of the nova explosion as a non-spherical fireball expanding at large velocities. (see Chesneau et al. 2007)

2.4 VLTI/AMBER interferometry and SIMECA radiative transfer gas modeling of the asymmetric disk of the Be star κ CMa

The geometry and kinematics of the circumstellar environment of the Be star κ CMa were studied in the Brγ emission line and its nearby continuum using the VLTI/AMBER instrument with a spatial resolution of about 6 mas and a spectral resolution of 1500. Our study focused on the kinematics within the disk and the determination of its rotation law. To obtain more kinematical constraints, we also used a high spectral resolution Paschen ß line profile obtained in December 2005 at the Observatorio do Pico do Dias, Brazil, as well as line profile variations and spectro-photometric data from the literature. Using wavelength-differential visibilities and differential phases across the Brγ line, we detected an asymmetry in the disk (Fig. 10). Moreover, we found that the AMBER data on κ CMa are difficult to interpret within the classical picture for Be stars; i.e., a fast-rotating B star close to its breakup velocity surrounded by a Keplerian circumstellar disk with an enhanced polar wind. (see Meilland et al. 2007)

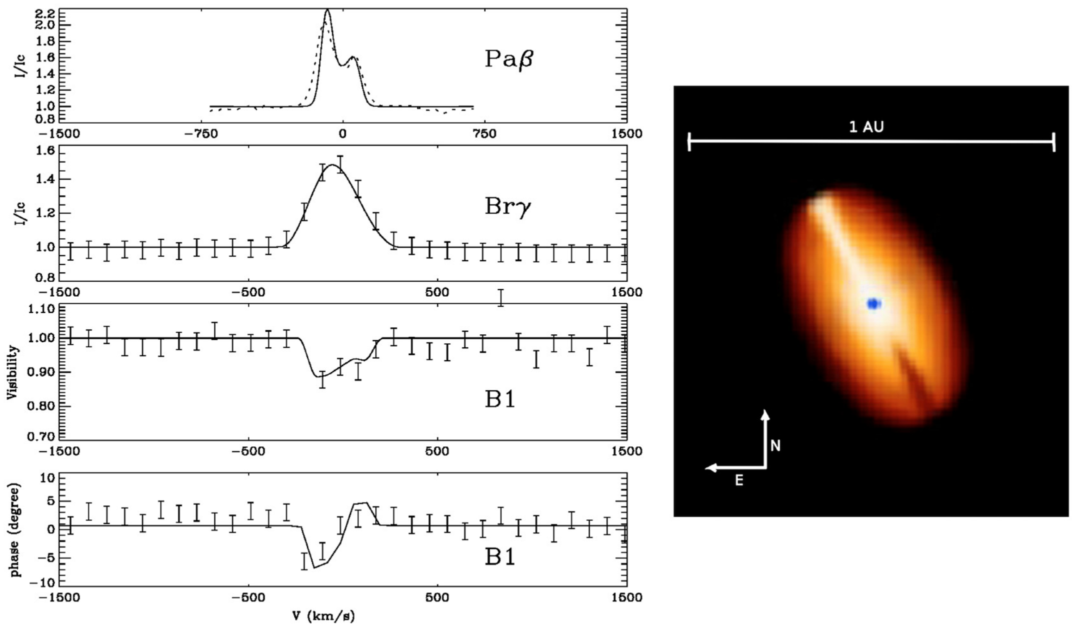

Figure 10 AMBER measurements of κ CMa. Left: From top to bottom: Paβ line profile (dotted line) with our best model fit (solid line), Brγ line profile, differential visibility, and differential phase for one of the 3 baselines. In each panel, the dots with errors bars show the VLTI/AMBER data and the solid line represents our best-fit SIMECA gas radiative transfer model. Right: Model intensity map of our best-fit SIMECA model in the continuum at 2.15 µm. The inclination angle is 60°. The central black spot represents the κ CMa photosphere (0.25 mas), and the bright part in the equatorial disk (N-E direction) indicates a region of enhanced gas density.

2.5 Gravitational-darkening of the rapidly rotating star Altair derived from near-infrared interferometry

Altair (=α Aql) is a bright, rapidly rotating, and pulsating A7 IV-V star of δ Scuti type. Spectroscopic and interferometric observations indicate a v_{eq} sin i value between 190 km s^{-1} and 250 km s^{-1} (e.g., Abt & Morrell 1995, ApJS 99, 135; Royer et al. 2002, A&A 393, 897). Theories suggest that such a high rotation velocity can lead to several modifications in the physical structure of a star like Altair. In particular, the star is expected (1) to be oblate due to a strong centrifugal force and (2) to exhibit gravity-darkening (von Zeipel 1924, MNRAS 84, 665). These theoretically expected modifications can now be measured with modern observing techniques, notably those based on long baseline interferometry. We performed a physically consistent analysis of all available interferometric data on Altair using our model for fast rotators (see Domiciano de Souza et al. 2002, A&A 393, 345). This model includes Roche approximation, limb-darkening (Claret 2000, A&A 363, 1081), and a von Zeipel-like gravity-darkening law. The rich observational set analyzed here includes data from VLTI/VINCI (V^2 in the H and K bands), as well as published data from PTI (V^2 in the K band) and NPOI (V^2, triple amplitudes, and closure phases in the visible between 520 nm and 850 nm). Our model shows that Altair exhibits a gravity-darkening $T_{eff} \propto g^{0.25}$, in agreement with theoretical predictions for hot stars (von Zeipel effect). We found that the observations of Altair are best reproduced by models with an intermediate inclination between 40° and 65°. (see Domiciano et al. 2005)

2.6 Confronting stellar model atmospheres with observations: VLTI/VINCI interferometry and UVES spectroscopy of the red giant Menkar

Coordinated near-infrared and optical spectroscopic observations of the M1.5 giant α Cet (Menkar) have been obtained with the instruments VINCI and UVES at the Paranal VLT Observatory. Spherically symmetric PHOENIX stellar model atmospheres are constrained by comparison to our interferometric and spectroscopic data, and high-precision fundamental parameters of Menkar are derived. Our high-accuracy VLTI/VINCI observations in the first and second lobes of the visibility function directly probe the model-predicted strength of the limb-darkening effect in the K band and the stellar angular diameter (Fig. 11). The high spectral resolution of UVES of R=80000−110000 allows us to confront observed and model-predicted profiles of atomic lines and molecular bands in detail.

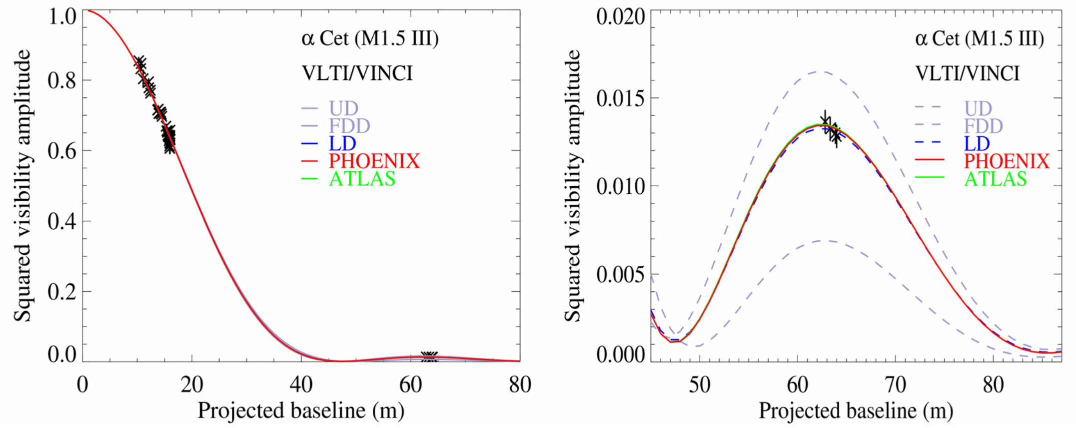

Figure 11 *Squared visibility amplitudes and error bars of α Cet obtained with VLTI/VINCI, together with best-fitting models of a uniform disk (upper dashed, light-blue line), a fully darkened disk (lower dashed, light-blue line), a parametrization $I=\mu^\alpha$ with α=0.24 (dashed blue line) and of PHOENIX and ATLAS 9 model atmosphere predictions (overlapping solid red and green lines, respectively). The PHOENIX and ATLAS 9 models shown have parameters T_{eff}=3800 K, log g=1.0, M=2.3 $M_\odot$. The left panel shows the full range of the visibility function, while the right panel is an enlargement of the obtained low squared visibility values in the 2nd lobe. Our measurements are significantly different from uniform disk and fully-darkened disk models, and in good agreement with the LD ($I=\mu^\alpha$), PHOENIX, and ATLAS 9 models.*

We show that our derived PHOENIX model atmosphere for Menkar is consistent with both the measured limb-darkening in the K band and the profiles of selected atomic lines and TiO bandheads from 370 nm to 1000 nm. At the level of our high spectral resolution, however, noticeable discrepancies between the observed and synthetic spectra exist. We obtain a high-precision Rosseland angular diameter of Θ_{Ross}=12.20±0.04 mas. Together with the Hipparcos parallax of 14.82±0.83 mas, this corresponds to a Rosseland radius of R_{Ross}=89±5 $R_\odot$, and together with the bolometric flux based on available spectrophotometry, to an effective temperature of T_{eff} =3795±70 K. The luminosity derived from these values is L=1460±300 $L_\odot$. Relying on stellar evolutionary tracks, these values correspond to a mass of M=2.3±0.2 $M_\odot$ and a surface gravity of log g=0.9±0.1. Our approach illustrates the power of combining interferometry and high-resolution spectroscopy to constrain and calibrate stellar model atmospheres. The simultaneous agreement of the model atmosphere with our interferometric and spectroscopic data increases confidence in the reliability of the modeling of this star, while discrepancies found at the detailed level of the high resolution spectra can be used to further improve the underlying model. (see Wittkowski et al. 2006)

2.7 Multi-epoch, multi-wavelength VLTI/MIDI and VLBA interferometry of the Mira variable S Ori: Unveiling the phase-dependent changes of the photosphere, molecular layer, dust shell, and SiO maser shell

To investigate the phase-dependent changes in the circumstellar environment of a Mira star, we carried out the first multi-epoch study that includes concurrent mid-infrared and radio interferometry. We obtained mid-infrared interferometry of S Ori with VLTI/MIDI in Dec 2004, Feb/Mar 2005, Nov 2005, and Dec 2005. We concurrently observed v=1, J=1−0 (43.1 GHz) and v=2, J=1−0 (42.8 GHz) SiO maser emission towards S Ori with the VLBA in Jan, Feb, and Nov 2005. The MIDI data were analyzed using self-excited dynamic model atmospheres including molecular layers, complemented by a radiative transfer model of the circumstellar dust shell. The VLBA data, on the other hand, allowed us to study the spatial structure and kinematics of the maser spots.

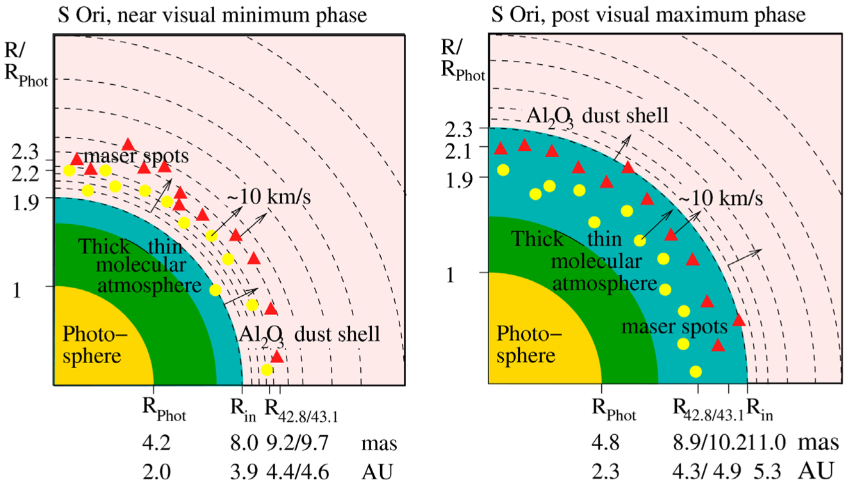

Figure 12 *Sketch of the radial structure of S Ori's circumstellar envelope at near-minimum (left) and post-maximum (right) visual phase, as derived from our work. Shown are the locations of the continuum photosphere (yellow), the molecular atmosphere which is optically thick in the N band (green), the molecular atmosphere which is optically thin in the N band (turquoise), the Al_2O_3 dust shell (dashed arcs), and the 42.8 GHz and 43.1 GHz maser spots (circles & triangles, respectively). The numbers below and beside the panels are the mean values of two epochs close to the minimum (left) and two epochs near the post-maximum (right) visual phase.*

The above-mentioned modeling of our MIDI data resulted in phase-dependent continuum photospheric angular diameters of 9.0±0.3 mas (phase 0.42; near minimum), 7.9±0.1 mas (phase 0.55), 9.7±0.1 mas (phase 1.16; post maximum), and 9.5±0.4 mas (phase 1.27). The dust shell can be modeled best with Al_2O_3 grains using phase-dependent inner boundary radii between 1.8 and 2.4 photospheric radii. The dust shell appears to be more compact with higher optical depth near visual minimum (τ_V~2.5) and more extended with lower optical depth after visual maximum (τ_V~1.5). The ratios of the 43.1 GHz/42.8 GHz SiO maser ring radii to the photospheric radii are 2.2±0.3/2.1±0.2 (phase 0.44), 2.4±0.3/2.3±0.4 (0.55), and 2.1±0.3/1.9±0.2 (1.15). The maser spots mark the region of the molecular atmospheric layers just beyond the steepest decrease in the mid-infrared model intensity profile. Their velocity structure indicates a radial gas expansion. S Ori shows significant phase-dependences of photospheric radii and dust shell parameters (see Fig. 12). Al_2O_3 dust grains and SiO maser spots form at relatively small radii of ~1.8−2.4 R_{phot}. The phase-dependent behaviour of the optical depth suggests that mass loss and dust formation are enhanced close to the surface near minimum visual phase, when Al_2O_3 dust grains are co-located with the molecular gas and the SiO maser shells. After the visual maximum, the dust shell is more extended. Silicon does not appear to be bound in dust, as our data show no sign of silicate grains. (see Wittkowski et al. 2007; ESO press release 25/07)

2.8 First multi-epoch VLTI/MIDI interferometry of the carbon-rich Mira star V Oph

The presence of the so-called "warm molecular layers" in O-rich AGB stars is now well-established, thanks to spectroscopic and interferometric observations. However, it is not clear whether or not such molecular layers exist for C-rich AGB stars. Spectro-interferometry across the C_2H_2 bands in the N band provides a unique opportunity to detect and characterize such C-rich molecular layers. Using VLTI/MIDI, we carried out multi-epoch N-band spectro-interferometric observations of the C-rich Mira variable V Oph at phases 0.18 (post-maximum), 0.49 (minimum light), and 0.65 (post-minimum).

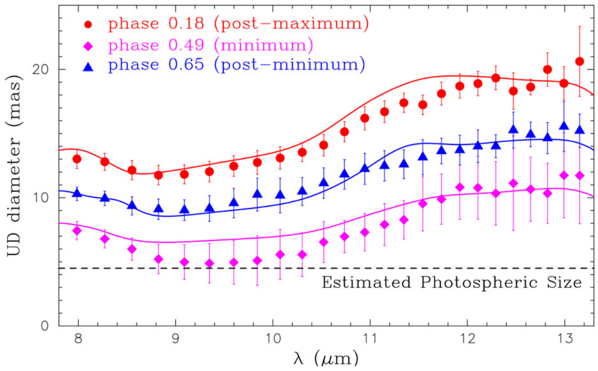

Figure 13 Left: Phase dependence of the N-band uniform-disk diameters observed with MIDI. The estimated photospheric size (~4.5 mas) is plotted by the dashed line. The solid lines represent the predictions by the C_2H_2 + dust shell model for the three epochs. Bottom: Temporal variations of the radii and column densities of the hot and cool C_2H_2 layers, and the optical depth of amorphous carbon dust in the dust shell.

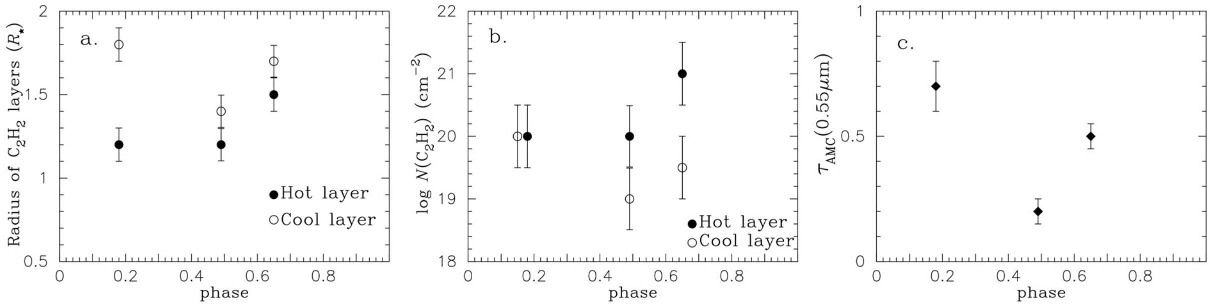

As shown in Fig. 13, all of the N-band uniform-disk diameters obtained are roughly constant between 8 and 10 μm and increase longward of 10 micron. As expected, these N-band angular sizes are significantly larger than the estimated photospheric size of V Oph. Also, our observations revealed, for the first time, that the object appears smaller at minimum (phase 0.49), with uniform-disk diameters of 5–12 mas (between 8 and 13 μm), than at phases before and after minimum (12–20 mas at phase 0.18 and 9–15 mas at phase 0.65). We interpret these results with a radiative tranfer model consisting of optically thick, hot and cool C_2H_2 layers and an optically thin dust shell containing amorphous carbon and SiC. Our modeling has revealed that the C_2H_2 layers are more extended (1.7–1.8 $R_\star$) at phases 0.18 and 0.65 than at phase 0.49 (1.4 $R_\star$) and that C_2H_2 column densities appear to be the smallest at phase 0.49 (Figs. 13a and 13b). On the other hand, no notable change was found for the temperatures of the C_2H_2 layers ($\sim$1000–1600 K). The dust shell's optical depths at phases 0.18 and 0.65 (0.5–0.7 at 0.55 μm) are higher than the value 0.2 derived for phase 0.49 (Fig. 13c). Our MIDI observations and modeling indicate that carbon-rich Miras also have extended layers of polyatomic molecules, as previously confirmed in oxygen-rich Miras. (see Ohnaka et al. 2007)

2.9 VLTI/MIDI interferometry of the circumbinary disk around the silicate carbon star IRAS 08002-3803 and 2-D radiative transfer modeling

Silicate carbon stars exhibit prominent silicate emission, despite their carbon-rich photospheres. It is believed that they have a low-luminosity companion and that oxygen-rich material was shed by mass loss when the primary star was an M giant. This O-rich material was stored in a circumbinary or circum-companion disk or torus until the primary star became a carbon star. We carried out the first N-band spectro-interferometric observations of a silicate carbon star, IRAS 08002-3803. Our MIDI observations revealed that the uniform-disk diameter is almost constant between 8-10 μm ($\sim$36 mas$\simeq$72 $R_\star$), while it steeply increases longward of 10 μm to reach ~53 mas (106 $R_\star$) at 13 μm (Fig. 14c). Radiative transfer modeling using our own 2-D Monte Carlo code (mcsim_mpi) shows that this result cannot be explained by a circumbinary or circum-companion disk consisting of only silicate because such models predict the angular size to be larger at 10 μm than at 8 μm due to a higher extended silicate emission at 10 μm.

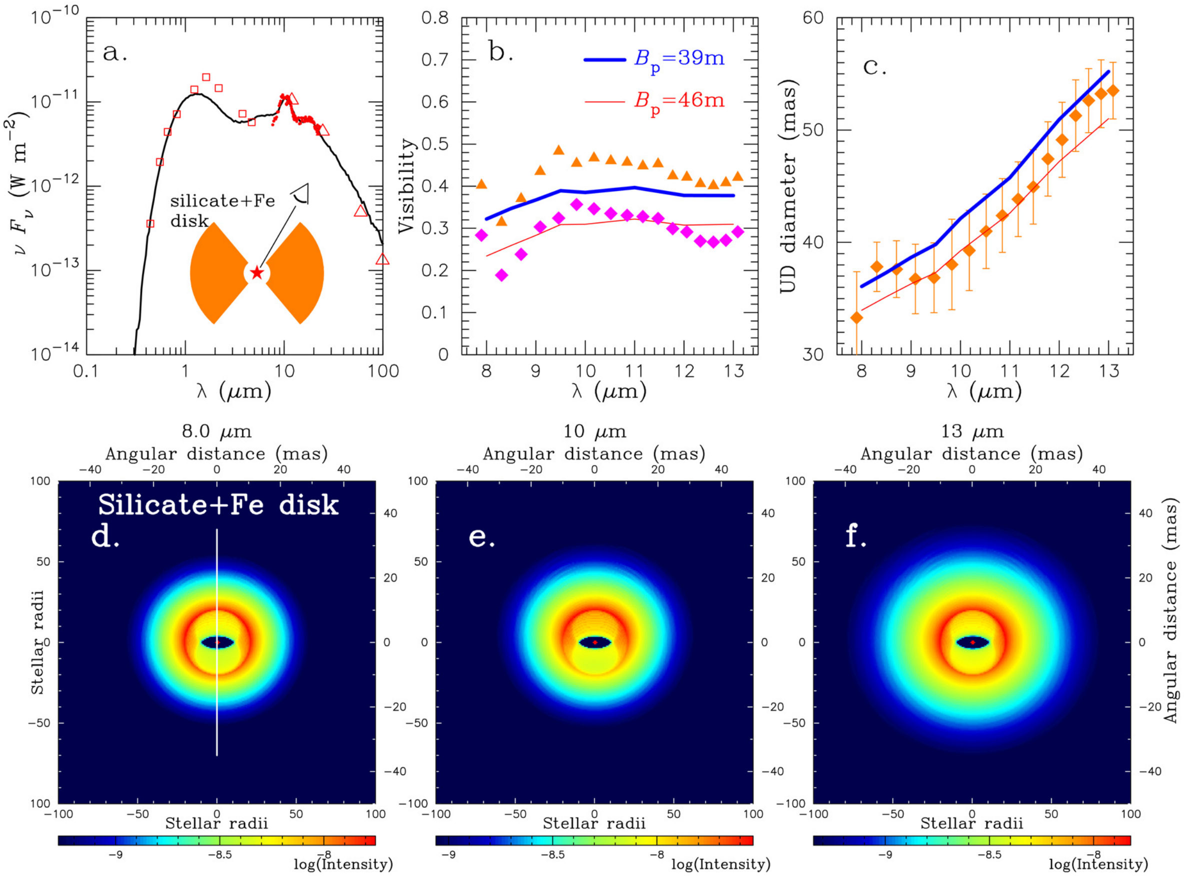

Figure 14 Radiative transfer modeling of the circumbinary disk of the silicate carbon star IRAS 08002-3803. The disk is optically thick (τ_V≈20 for silicate and ~3 for metallic iron) with a half-opening angle of 50° and an inner boundary radius of 20 $R_\star$ (40 AU), viewed from an inclination angle of 30° (see the inset in a.). a) The observed SED: open squares, open triangles, and dots. The model SED: solid line. b) Filled triangles and diamonds: MIDI visibilities measured with 39 m and 46 m baselines, respectively. The thick and thin solid lines represent the corresponding model visibilities. c) Filled diamonds: observed uniform-disk diameters. Thick and thin solid lines: uniform-disk diameters predicted by the model for a baseline length of 39 and 46 m, respectively. d-f) The mid-infrared model images of the disk predicted by the silicate+ metallic iron model for 8, 10, and 13 μm. The solid line in d illustrates the orientation of the baseline vector used in the calculation of the visibilities.

Our modeling suggests that an optically thick circumbinary disk with two grain species — small silicates and a second grain species such as amorphous carbon, large silicate grains, or metallic iron grains — can explain the observations. As an example, the silicate+metallic iron disk model is shown in Fig. 14. This model can fairly reproduce the observed SED and the N-band visibilities, while the model visibilities are still somewhat too flat compared to the MIDI observations. Figures 14d–f also illustrate that the 13 μm model image is more extended than the images at 8 and 10 μm, in agreement with the observed wavelength dependence of the uniform-disk diameter. (see Ohnaka et al. 2006)

2.10 VLTI/MIDI mid-infrared interferometry and 2-D gas radiative transfer modeling of a Be star: The innermost circumstellar environment of α Arae

Be stars are hot, massive stars characterized by rapid rotation and a dense, circumstellar gas environment which is the source of the observed strong line emission. To better understand the physical conditions and the spatial distribution of the circumstellar gas around Be stars, we carried out VLTI/MIDI observations of the Be star α Arae in the wavelength range from 8 to 13 μm. The MIDI measurements show that α Arae's circumstellar disk is nearly unresolved in the mid-infrared using projected baselines of 102 m and 74 m. Using a simple uniform-disk model, the MIDI observations show that α Arae's envelope has an N-band diameter of 4±1.5 mas. This corresponds to 14 $R_\star$, assuming $R_\star$=4.8 $R_\odot$ and the Hipparcos distance of 74 pc.

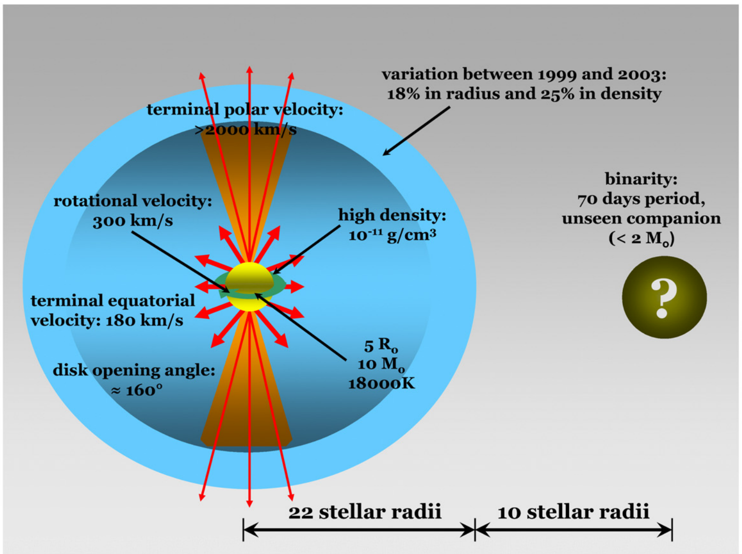

Figure 15 Schematic view of α Arae's circumstellar environment, as modeled with the SIMECA gas radiative transfer code.

The disk density must be large enough to produce the observed strong Balmer line emission. In order to determine the stellar parameters and the physical conditions within the circumstellar gas envelope of α Arae, we used the 2-D gas radiative transfer code SIMECA (Stee & Bittar 2001, A&A 367, 532). Optical spectra taken with the Échelle instrument HEROS and the ESO-50 cm telescope, as well as infrared spectra obtained with the 1.6 m Brazilian telescope, were included for the modeling, together with the MIDI spectra and visibilities. These observations put complementary constraints on the density and geometry of α Arae's circumstellar disk (Fig. 15). We investigated the potential truncation of the disk by a companion and found spectroscopic indications of a periodic perturbation of some Balmer lines. (see Chesneau et al. 2005)

2.11 The nebula Frosty Leo: Diffraction-limited bispectrum speckle interferometry, AO imaging polarimetry, and radiative transfer modeling in polarized light

The central stars in proto-planetary nebulae (PPN) have a low to intermediate initial mass (~1–8 $M_\odot$). They are excellent astrophysical laboratories for studying the physical processes which drive stellar winds and mass loss. It is thought that a PPN, with its characteristic shape, rapidly develops after the end of the AGB phase. A large fraction of PPNs exhibit a bipolar or point-symmetric morphology, while the dust shells formed in the previous evolutionary stage by the intensive mass loss around AGB stars are nearly spherical. Understanding the physical mechanisms of PPN formation and the transition from a spherical to a non-spherical shape of the circumstellar environment are two important research goals.

We obtained K′-band bispectrum speckle interferometric images and HK-band polarimetric images of Frosty Leo using the ESO 3.6 m telescope and the CIAO AO system on the 8 m Subaru telescope, respectively. The diffraction-limited speckle image with 0.″12 resolution (Fig. 16, top-left frame) clearly shows clumpy structures in the bipolar lobes and the dust lane between the lobes. Our AO polarization map (top right) displays the polarization disk between the bipolar lobes, implying that the equatorial region is optically thick. Furthermore, an elongated region with low polarization at position angle −45° is detected. It is likely a tube-like structure with low densities, probably carved out by a jet (Sahai et al. 2000, A&A 360, L9). For a quantitative interpretation of our observations, we performed radiative transfer modeling of the Frosty Leo nebula, including polarization. We found that a model with a single grain species can reproduce the SED and the observed K′-band image, but fails to simultaneously reproduce the measured polarization map. Good simultaneous agreement with the SED, the observed K′-band image, and the polarization pattern was only achieved when two distinct grain species were considered in the radiative transfer model (see bottom panels in Fig. 16): micron-sized grains (0.5 to 2.0 μm in radius) in the equatorial high-density region and sub-micron-sized grains (0.005 to 0.8 μm) in the polar region. Our study illustrates that polarization measurements and radiative transfer modeling of polarized light are of great importance for an improved understanding of the physical conditions in the complex circumstellar environment of PPNs.

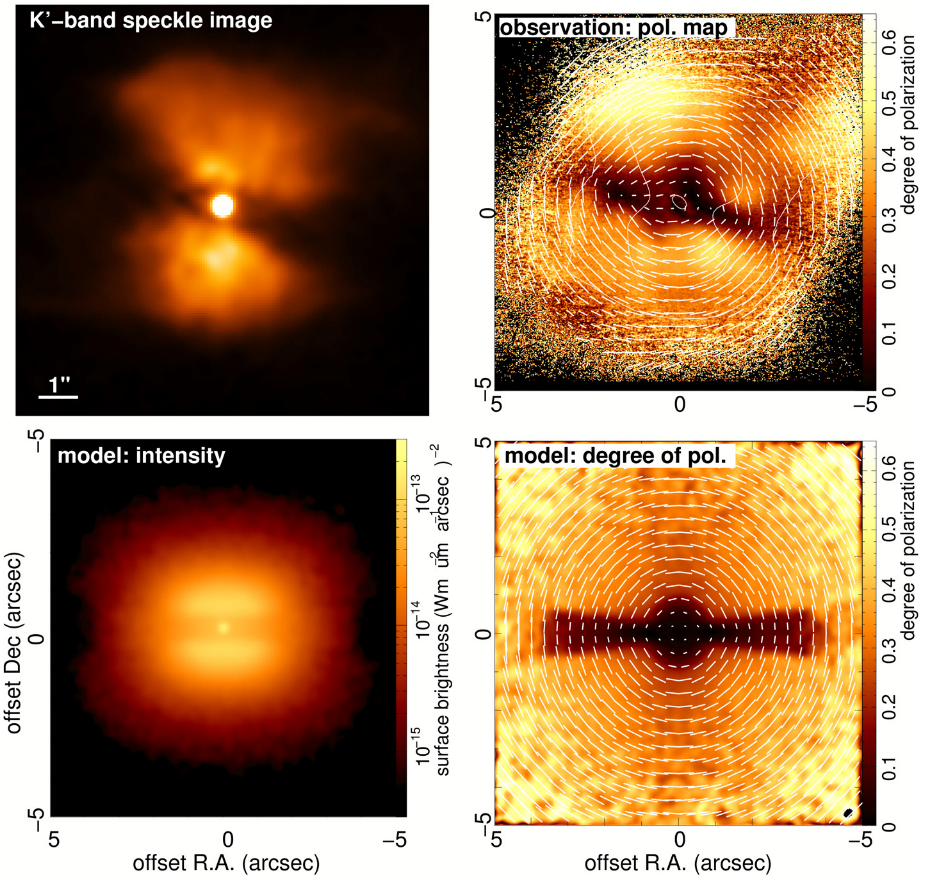

Figure 16 Diffraction-limited K'-band speckle image of Frosty Leo (top left) and observed polarization map (top right) showing the polarization vectors (i.e. degree of polarization and position angle of the electric field) and the degree of polarization (heat image). The K-band intensity image and the degree of polarization of our radiative transfer model are shown in the bottom panels.

In addition to Frosty Leo, we also investigated a sample of 19 other PPNs and AGBs using HST/NICMOS and 8 m Subaru AO observations for statistical studies on PPN morphology. (Murakawa et al. 2007, A&A submitted (Frosty Leo); see Ueta el al. 2007; Murakawa et al. 2007)

2.12 Proper motion measurements of dust shell structures in the Egg nebula

The Cygnus Egg nebula (=AFGL 2688) is one of the most extensively studied, carbon-rich, bipolar proto-planetary nebulae. From radiative transfer modeling (Lopez & Perrin 2000, A&A 354, 657), the total envelope mass was estimated to be 7 $M_\odot$, assuming a distance of 1.0 kpc. However, stellar evolution theory predicts that for AGB stars with an initial mass higher than ~5 $M_\odot$, hot-bottom-burning prevents the formation of carbon stars. One possible reason for such contradictory results in the case of the carbon-rich nebula AFGL 2688 may be a mass overestimation due to the assumed distance of 1.0 kpc.

In order to re-determine the distance to the Egg nebula, we measured the proper motion of the local dust shell structures in the nebula. We used archival data taken with the HST/NICMOS camera from two different epochs, covering a 5.5-yr interval, derived the position displacement of corresponding local structures, and found that the dust shell is expanding with a proper motion of 17 mas yr^{-1} (see Fig. 17). With a deprojected outflow velocity of 45 km s^{-1} and an inclination angle of 7.7° derived from CO measurements (Cox et al. 2000, A&A 353, L28), we determined a distance of approximately 420 pc. The refined distance estimate yields a luminosity of the central star of 3.3×10^3 $L_\odot$, a total shell mass of 1.2 $M_\odot$, and a mass-loss rate of 3.6×10^{-3} $M_\odot$ yr^{-1}. Assuming 0.6 $M_\odot$ as the mass of the central post-AGB star, the initial stellar mass is 1.8 $M_\odot$. The results of this project are consistent with stellar evolution models of stars with initial masses ≤3 $M_\odot$, which likely become carbon stars in the advanced phase of their AGB evolution. (see Ueta et al. 2006)

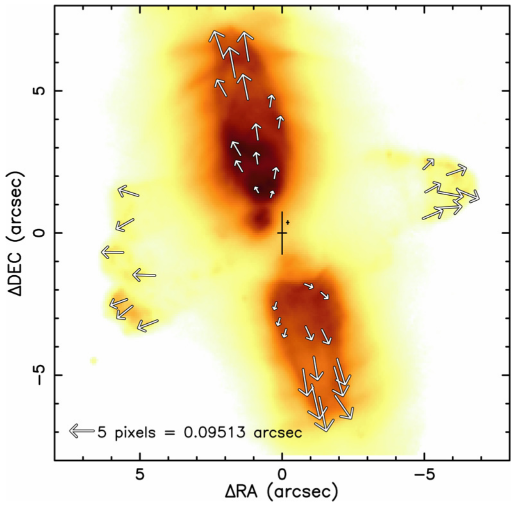

Figure 17 *Measured proper motions in the Egg nebula. The heat image is one of two HST/NICMOS K-band images separated 5.5 yrs in time. The arrows indicate the displacement of the local dust shell structures within the 5.5-yr interval. The cross indicates the position of the central star. From the proper motions and the radial velocities obtained from CO measurements, the distance to the Egg nebula was determined to be 420 pc, a factor of ~2.5 smaller compared to previous estimates.*

2.13 Near-infrared speckle interferometry and radiative transfer modeling of the highly dust-enshrouded carbon star LP And

Using the BTA 6 m telescope, we carried out near-infrared speckle interferometric observations of the carbon star LP And in the H and K′ bands with diffraction-limited resolutions of 56 and 72 mas, respectively, and analyzed the visibilities and the spectral energy distribution of this carbon star by means of extensive 2-D radiative transfer modeling to determine the physical parameters of its dusty envelope. The observed visibility of LP And reveals a spherically symmetric envelope surrounding the central star. The SED of LP And in the entire range from the near-IR to millimeter wavelengths and our H-band visibility can be reproduced by a spherical dust envelope with parameters very similar to those of CW Leo (IRC+10 216), the best-studied carbon star (Fig. 18). For the newly estimated pulsation period P=617±6 days and distance D=740±100 pc, we found that LP And changes its luminosity between 16200 and 2900 $L_\odot$, its effective temperature between 3550 and 2100 K, and its radius $R_\star$ between 340 and 410 $R_\odot$ throughout a full pulsation cycle.

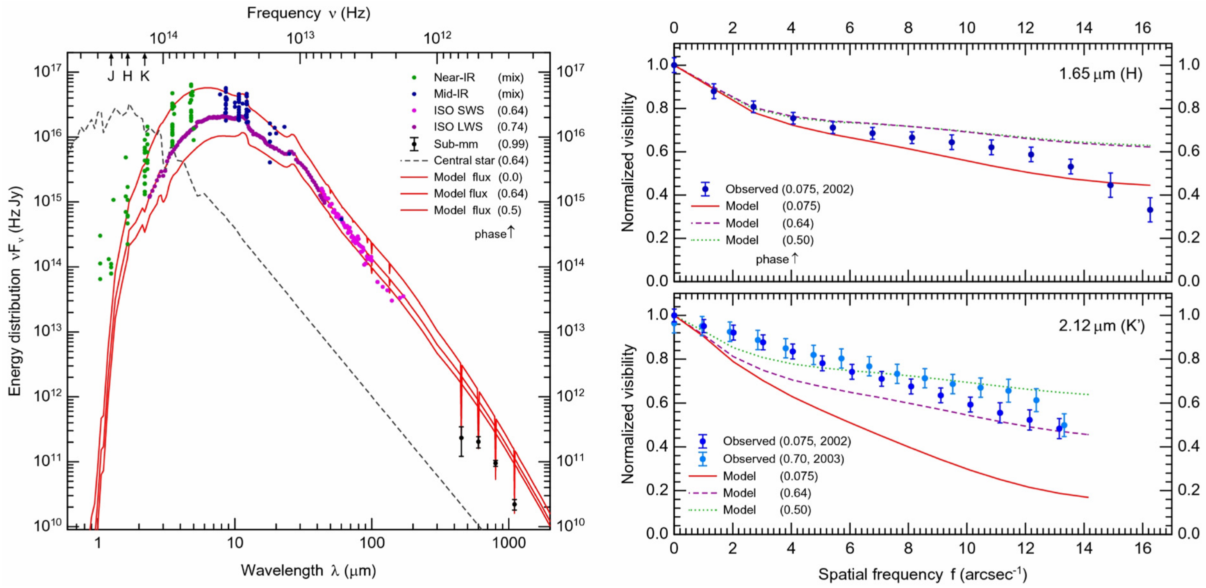

Figure 18 *Left: Observed SED of LP And compared to our model at three different phases (ø=0.0, 0.5, and 0.64). Right: Model visibilities of LP And in the H and K′ bands (phases ø=0.08, 0.50, and 0.64) compared to the azimuthally averaged visibilities from our speckle-interferometry data obtained in 2002 and 2003 (ø=0.08 and 0.70).*

Our best model gives a mass-loss rate of $dM/dt \approx 1.9 \times 10^{-5}\ M_\odot\ yr^{-1}$. The inner boundary of the dusty envelope is located at 2 stellar radii. The total mass of the envelope lost by the central star is $M = 3.2\ M_\odot$, assuming a dust-to-gas mass ratio of $\rho/\rho_d = 0.004$. The dust model contains small silicon carbide grains, inhomogeneous grains made of a mixture of SiC and incomplete amorphous carbon, and thin mantles made of iron-magnesium sulfides. We find that our K′-band visibility could not be fitted by our spherical model. If slight deviations from spherical geometry in LP And's circumstellar envelope are the reason, then the object's evolutionary stage would be even more similar to that of CW Leo. Our study shows that LP And appears to be a highly-evolved intermediate-mass star (initial mass $M_\star \approx 4\ M_\odot$) at the end of its AGB phase. (see Mensh'chikov et al. 2006)

2.14 High-resolution spectroscopy for the distance determination of Cepheids: A period-projection factor relation

Near-infrared interferometry provides a new, quasi-geometrical way to determine the distance of Galactic Cepheids up to 1 kpc. The basic principle of the Interferometric Baade-Wesselink method (IBW) is to compare the linear and angular size variation of a pulsating star in order to derive its distance. The key point is that interferometric measurements in the continuum lead to angular diameters corresponding to the photospheric layer, while the linear stellar radius variation is deduced by spectroscopy; i.e., based on line-forming regions located higher in the atmosphere. The spectral line profile is indeed critically affected by the dynamical structure of a Cepheid's atmosphere (right panel in Fig. 19). Thus, radial velocities measured from line profiles, hereafter V_{rad}, include the integration in two directions: over the surface through limb-darkening and over the atmospheric layers through velocity gradients.

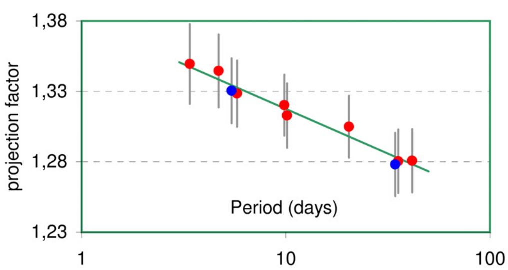

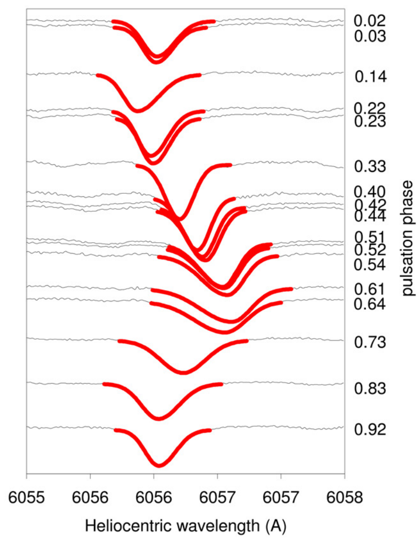

Figure 19 *Right: HARPS spectral line profiles of β Dor (spectral resolution R≈120000) together with a modeled bi-gaussian (in red) at different pulsation phases. Left: Considering different spectral lines which form at different levels in the atmosphere, the projection factor is derived as a function of the logarithm of the period. Blue and red points correspond to HARPS observations and models, respectively.*

Since the work of Nardetto et al. (2004, A&A 428, 131), all these phenomena have been merged into one specific quantity, generally considered to be constant with time: the projection factor p, defined as $V_{puls} = pV_{rad}$, where V_{puls} is defined as the photospheric pulsation velocity. V_{puls} is then integrated with time to derive the photospheric radius variation. Computing hydrodynamical models for δ Cep and ℓ Car, we validate a new spectroscopic method for determining the projection factor. This method is applied to eight stars observed with the HARPS spectrometer. We divide the projection factor into three sub-concepts : (1) a geometrical effect, (2) the velocity gradient within the atmosphere, and (3) the relative motion of the optical pulsating photosphere compared to the corresponding mass elements. Both (1) and (3) are deduced from geometrical and hydrodynamical models, respectively, while (2) is derived directly from spectroscopic observations considering different lines forming at different levels in the atmosphere, which allows us to probe velocity gradients. We found, for the first time, a period-projection factor relation (hereafter Pp; Fig. 19 left). This Pp relation is an important tool for removing a bias in the calibration of the period-luminosity (PL) relation of Cepheids. If a constant projection factor (generally p=1.36 for all stars) is used to derive the PL relation, errors of 0.10 and 0.03 magnitudes on the slope and zero-point of the PL relation, respectively, can be introduced. Our Pp relation was recently confirmed by HST observations. (see Nardetto et al. 2007; Fouqué et al. 2007, accepted)

3 DATA PROCESSING

3.1 Reconstruction of aperture synthesis images from LBT LINC-NIRVANA data using the Richardson-Lucy and space-variant Building Block Method

The Large Binocular Telescope (LBT) with its two 8.4 m mirrors is being built on Mt. Graham, Arizona. One of the instruments of the LBT is the optical/NIR beam combiner instrument LINC-NIRVANA. This instrument is being built by a consortium including the MPI for Astronomy (PI institute), the University of Cologne, the Arcetri Observatory in Florence, and our institute. Due to the two 8.4 m mirrors of the LBT, the raw images obtained with LINC-NIRVANA will have, in one direction, the spatial resolution equivalent to a diffraction-limited 8.4 m single-dish telescope, and in the orthogonal direction, that of a 22.8 m telescope. Important characteristics of the instrument will be the large field-of-view of 10" and the high sensitivity. Within the LINC-NIRVANA project, the MPIfR group is responsible for the fringe tracker detector system and the complete image reconstruction software.

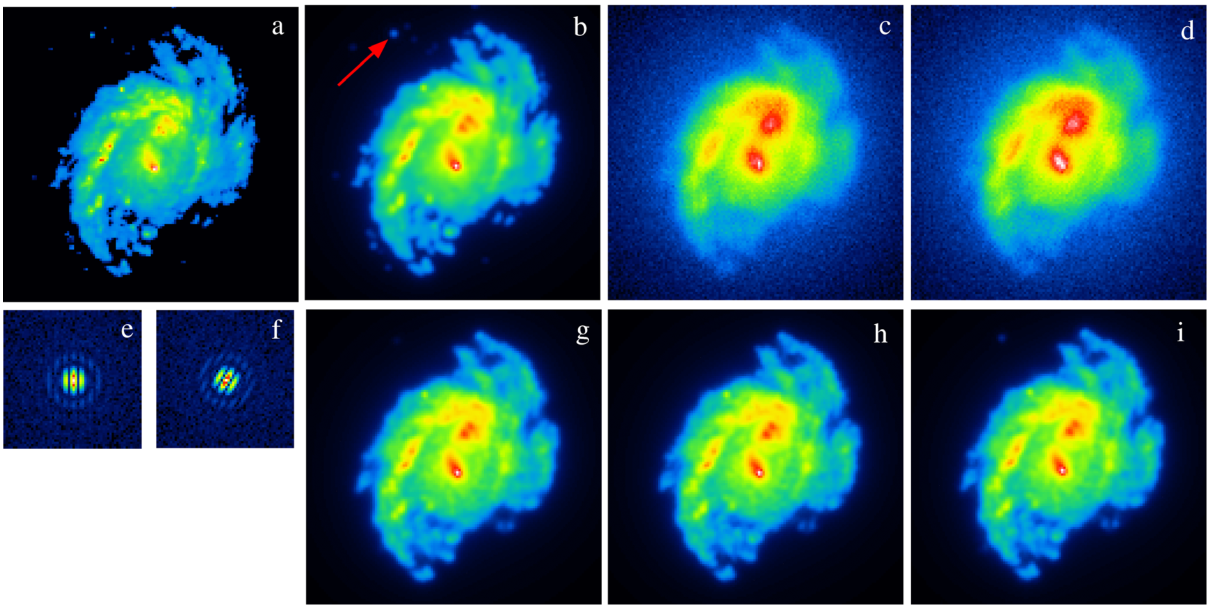

Figure 20 *Reconstruction of aperture-synthesis images from computer-simulated LBT raw data (all images are shown on the same scale). a: test object; b: object convolved with the PSF of a simulated diffraction-limited 22.8 m telescope; c, d: computer-simulated LBT raw images of the object (simulated total magnitude $J=17^m$, sky background $J=16^m$ per arcsec square, read-out noise of 11 electrons rms, pupil position angles 0° and 30°); e, f: LBT PSFs for position angles 0° and 30°. These PSFs are derived from unresolved stars in the vicinity of the target. The brightness of these reference stars ranges from $J=20^m$ to 21^m; g, h, i: diffraction-limited images reconstructed from 6 LBT raw images (taken with pupil position angles of 0°, 30°, 60°, 90°, 120°,and 150°, two of which are shown in panels c and d and the corresponding 6 LBT PSFs (two of which are shown in panels e and f) using the RL (g), the OSEM (h), and the BB (i) methods. The faint star-like structure in the upper left corner of panels a and b (marked by an arrow in panel b) has a brightness of $J=25^m$. The restoration errors are 5.4% (g), 5.6% (h), and 5.2% (i).*

In the framework of the LINC-NIRVANA project, we developed a new image reconstruction method: the regularized and space-variant Building Block method, which is able to reconstruct diffraction-limited aperture-synthesis images from LBT LINC-NIRVANA data. Images with the diffraction-limited resolution of a 22.8 m single-dish telescope can be derived if raw images are taken at several different hour angles.

We simulated computer-generated and laboratory LBT interferograms that are similar to the data which will be obtained with the LINC-NIRVANA beam combiner instrument. From the simulated data, diffraction-limited images were reconstructed with the Richardson-Lucy (RL) method (Richardson 1972, J. Opt. Soc. Am. 62, 55), the Ordered Subsets Expectation Maximization (OSEM) method (Hudson & Larkin 1994, IEEE Trans. Med. Imag. 13, 601) and the regularized Building Block (BB) method, which is an extension of the Building Block method (Hofmann & Weigelt 1993, A&A 278, 328). All three methods used within our study are able to reconstruct diffraction-limited images with almost the same quality. Our image reconstruction studies were performed with computer-simulated J-band (see Fig. 20) and laboratory H-band raw data of a galaxy with simulated total magnitudes of $J=16-18^m$ and $H=16-19^m$, respectively. One of the faintest structures in the computer-generated images has a brightness of $J\sim25^m$ (see arrow in Fig. 20b). The simulated reference stars within the isoplanatic patch have magnitudes of $J=20-21^m$ and $H=19^m$, respectively. The restoration errors for the RL, OSEM, and BB reconstructions shown in Fig. 20 are 5.4% (g), 5.6% (h), and 5.2% (i), respectively. Furthermore, to take into account the large field-of view of LINC-NIRVANA, raw data with space-variant point spread functions were simulated, and diffraction-limited images were reconstructed using the space-variant version of the Building Block method. (see Hofmann et al. 2005)

4 ACTIVE GALACTIC NUCLEI IN THE INFRARED

4.1 A new method for 3-D radiative transfer modeling of clumpy AGN dust tori

The optically and geometrically thick dust torus is a cornerstone in unification schemes for AGN. Its orientation towards the observer explains the difference between type 1 and type 2 objects: In type 2 AGN, the dust torus obscures the line-of-sight towards the central AGN accretion disk and broad-line region (BLR). The torus absorbs most of the direct optical and UV radiation of the AGN and re-emits the received energy in the infrared. When seen face-on (type 1 AGN), the hot dust in the innermost torus region is visible, which can result in the appearance of a silicate emission feature at ~10 µm. In edge-on geometries, the near-IR SED is very red and the silicate feature appears in absorption. Several radiative transfer models have been presented where the dust in the torus is smoothly distributed. These models, however, show redder NIR colors for type 2 AGN than what has been observed. In addition, the observed silicate features in absorption and emission are weak, although models would predict them to be pronounced. It has been suggested that these problems can possibly be overcome by distributing the dust in the torus in discrete dust clouds.

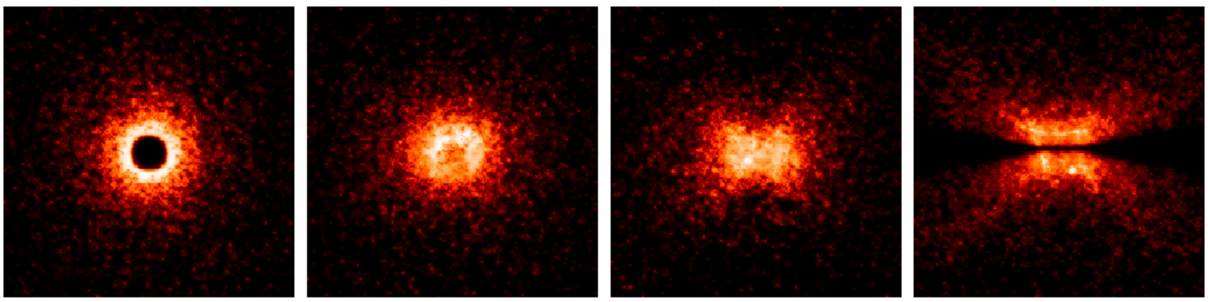

Figure 21 *L-band model images of a clumpy torus with a random arrangement of dust clouds. From left to right: Brightness distribution of the clumpy torus for inclinations i=90° (face-on), 45°, 0° (edge-on), and 0° with an anisotropic central source, respectively. The size of the torus scales with the sublimation radius (the diameter of inner torus ring in the left image is 2 sublimation radii). The "graininess" in the images originates from the clumpy structure of the torus.*

We developed a method to model the near- and mid-infrared emission of AGN with a 3-dimensional radiative transfer model of clumpy tori. The model combines high-precision Monte Carlo simulations of dust clouds and fast ray-tracing methods of the emission of $\sim10^4$ individual clouds, which are summed up to obtain images and SEDs of the torus. The properties of the individual dust clouds are taken from a physically motivated description of self-gravitating and shear-limited clouds in the gravitational potential of a supermassive black hole. In a first step, the radiation fields of the individual clouds are simulated at

various distances from the AGN with our Monte Carlo code. For that, we account for different types of heating: (1) direct illumination by the AGN or (2) heating by diffuse radiation from surrounding clouds. In a second step, these clouds are distributed within the torus region and their emission is added to the final torus spectrum, as seen by the observer. It has been demonstrated that clumpiness in AGN tori can overcome the described problems of previous torus models. Furthermore, we found out that the actual 3-dimensional distribution of dust clouds has a significant impact on the SEDs, images, and visibilities.
In Fig. 21, we present L-band model images of a clumpy torus. The "graininess" in the images is a direct result of the clumpy structure of the torus. (see Hönig et al. 2006)

4.2 NGC 1068: First radiative transfer modeling of all interferometric observations in the IR

Diffraction-limited near-infrared images of the type 2 AGN in NGC 1068 obtained with bispectrum speckle interferometry show an extended nucleus of 18×39 mas (1.3×2.8 pc) in the K band and 18×45 mas in the H band (Weigelt et al. 2004, A&A 425, 77). Furthermore, it was possible to resolve the nuclear mid-IR emission using the VLTI/MIDI instrument (Jaffe et al. 2004, Nature 429, 47). Visibilities in the 8−13 μm range show that the silicate absorption feature at 42 m and 78 m baseline length is more prominent than in the total flux. We applied our clumpy torus model to our above-mentioned near- and mid-IR interferometric observations of the NGC 1068 nucleus. It was possible, for the first time, to simultaneously reproduce both the SED and all IR observations. In Fig. 22 (left) we compare the high-spatial resolution (small aperture) SED of NGC 1068 with our clumpy torus model. The AGN luminosity inferred from our model is 2×10^{45} erg s^{-1}. The torus has a constant relative scale height and is seen almost edge-on. The model SED in the near-IR is in good agreement with the observed near-IR color. In the mid-IR, the modeled moderate silicate absorption feature reproduces the observed N-band spectrum.

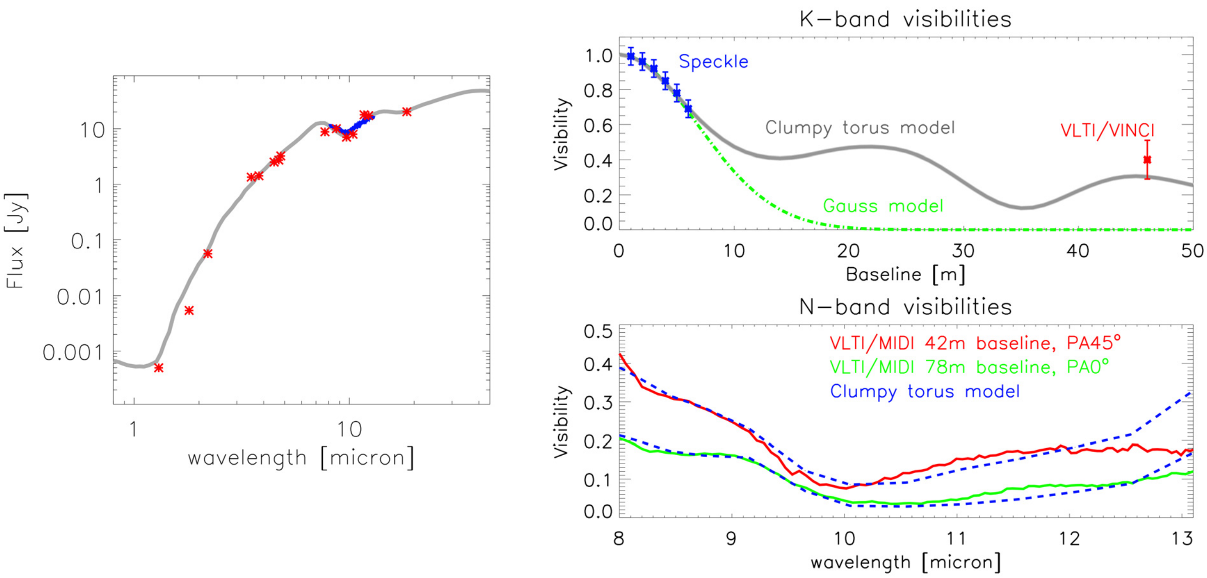

***Figure 22** Left: Comparison of the observed SED of NGC 1068 (red asterisks: photometry; blue line: MIDI total flux) with our clumpy torus model (grey line); Right: Observed and modeled K and N-band visibilities of NGC 1068. Top right: Comparison of observed speckle and long-baseline K-band interferometric visibility and predictions of our clumpy torus model. Bottom right: Comparison between the VLTI/MIDI spectro-interferometry of NGC 1068 for two different baselines (solid lines) and our clumpy torus model (dashed lines).*

In Fig. 22 (right), we compare all observed K- and N-band visibilities with our model. The clumpy torus model follows the trend of deeper silicate absorption features at longer baselines, as observed with MIDI (Fig. 22, bottom right). We also show that the surprisingly high visibility observed with VLTI/VINCI in the K band (V=0.4±0.1 at the 46 m baseline; Wittkowski et al. 2004, A&A 418, L39) is probably the result of a clumpy structure inside the torus (Fig. 22, top right). Other possibilities for interpreting the high K-band visibility involve contamination by a synchrotron source or the accretion disk seen directly through torus "holes". (see Hönig et al. 2006)

4.3 NGC 3783: First mid-infrared spectro-interferometry of a type 1 AGN

Using VLTI/MIDI spectro-interferometry in the wavelength range of 8-13 μm, we resolved, for the first time, the MIR nucleus of a Seyfert type 1 galaxy. We obtained spectra and visibilities of NGC 3783 for baselines of 65 and 69 m (see Fig. 23) at two different position angles. The spectrum shows a very weak silicate feature in emission at 9.7 μm and a general flux increase towards longer wavelengths. The derived visibilities (Fig. 23, right) are in the range of 0.4 to 0.6. The modeling results show that the SED and visibility can approximately be reproduced by a clumpy torus model seen face-on (blue lines in Fig. 23). The most striking property of the model is a very low surface filling factor of emitting clouds. The mid-IR emitting region of the torus extends from the inner sublimation radius of 1.2 mas outwards to at least 50 mas.

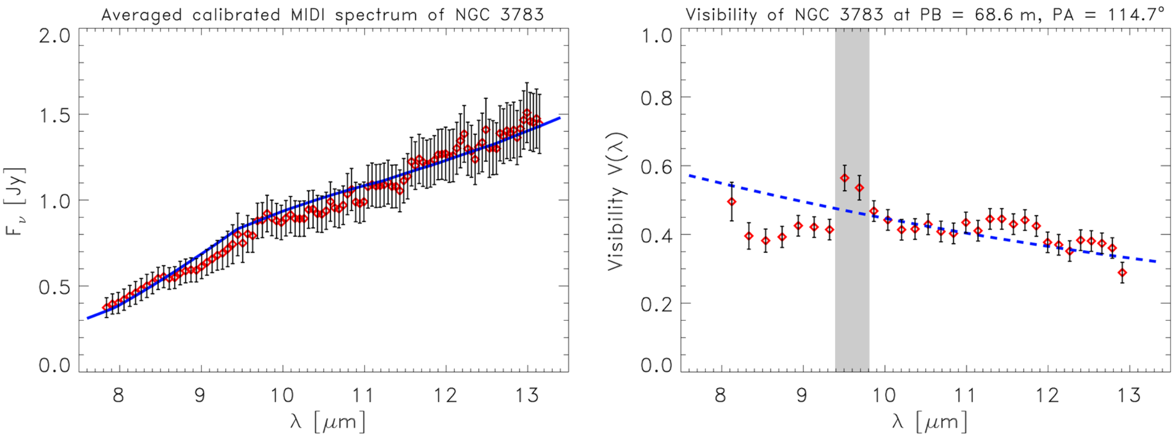

Figure 23 *Mid-IR long-baseline spectro-interferometry of NGC 3783 with VLTI/MIDI. Comparison of the observed total flux spectrum (left, red diamonds) and visibilities (right, red diamonds) with a clumpy torus model (blue lines) in the wavelength range of 8-13 μm.*

Furthermore, we resolved the nucleus of the Circinus galaxy using the ESO 3.6 m telescope and K-band bispectrum speckle interferometry. The reconstructed diffraction-limited image shows an elongated structure along the outflow. More recently, we also resolved the faint type 2 AGN in NGC 424 with MIDI. Both NGC 3783 and NGC 424 are among the faintest targets so far observed with VLTI/MIDI, with correlated fluxes of $\sim$ 0.3 Jy. (Beckert et al., in preparation)

4.4 The nature of obscuration in hidden QSOs

One of the major astronomical discoveries in the last few years was the identification of type 2 counterparts of QSOs by several X-ray surveys with XMM and Chandra. These objects were considered the “missing link” in the unification scheme of AGN. Follow-up observations with Spitzer allowed for establishing rest-frame near- to mid-IR SEDs of the type 2 QSOs to study the origin of the nuclear obscuration. We used our clumpy torus model to interpret a sample of 21 type 2 QSOs. This sample includes the most luminous obscured objects known to date. By modeling the IR SED, we confirmed that $\sim$2/3 of the QSOs are obscured by the nuclear dust torus. On the other hand, for some of the type 2 QSOs, the observed blue NIR colors seem to be inconsistent with the deep silicate absorption features present at 9.7 μm. The rest-frame SEDs of these objects at optical and infrared wavelengths are shown in Fig. 24. Based on detailed modeling with our torus model, we argue that a second dust component is required to explain the observed spectral features in these type 2 QSOs. This component can be described as a cold absorber. It is probably linked to the host galaxy and detached from the immediate nuclear vicinity. Thus, it is possible that the tori in these particular obscured QSOs are seen face-on, while a cold absorber in the host galaxy produces deep silicate absorption features. Our model results are shown in Fig. 24 and suggest that the cold absorber might be responsible for the deep silicate absorption features and the optical/UV obscuration in $\sim$1/3 of the type 2 QSOs. (see Polletta et al. 2007)

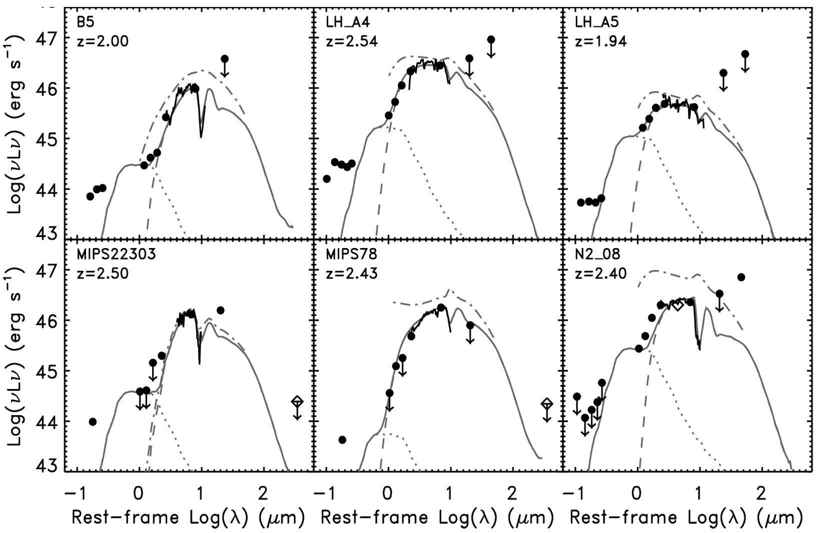

Figure 24 *Rest-frame SED of 6 of the obscured QSOs (black dots) and best-fit models (solid grey curve) obtained from a torus+cold absorber model (dashed grey curve) and an elliptical galaxy template (dotted grey curve). The dot-dashed curve represents the torus model in the 1−50 µm range before introducing the cold absorber.*

4.5 The AGN–torus connection

We studied the feedback of AGN radiation on the dust torus. The torus is presumably the matter reservoir for feeding the accretion disk. By comparing the influence of radiation on dust grains and dust clouds, we found out that dust which is smoothly distributed in the torus cannot be gravitationally bound against the radiation pressure from the AGN. On the other hand, if the dust is arranged in self-gravitating clouds, the received momentum from the radiation of the accretion disk is efficiently diluted and dispersed inside the cloud, so that the dust and associated gas can be accreted inwards to supply the AGN.

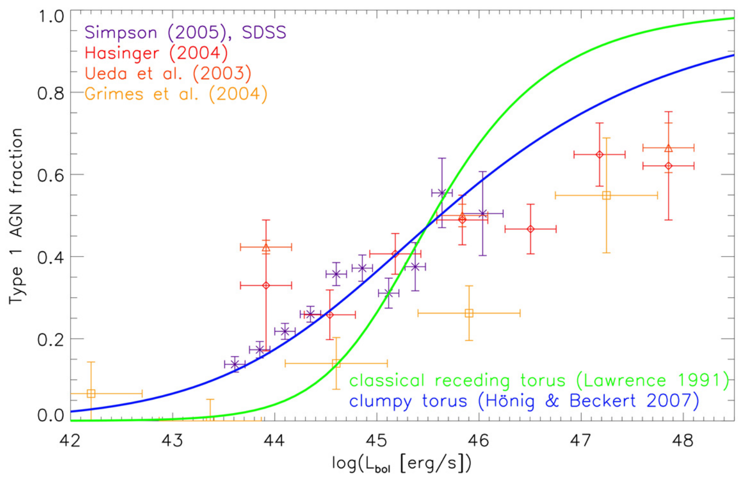

Figure 25 *Change of the fraction of type 1 AGN with luminosity, as predicted by our clumpy torus model (blue line) and the original receding torus model (green line; Lawrence 1991, MNRAS 360, 565). Observational results from various surveys are overplotted for comparison.*

In a next step, we used the physically motivated accretion scenario for clumpy dust tori from Beckert & Duschl (2004, A&A 426, 445) to study the impact of the AGN radiation on obscuration properties of the torus. We showed that below an AGN luminosity of $\sim 10^{42}$ erg s^{-1}, low accretion rates can no longer support the existence of an obscuring torus. It is expected that for lower luminosities, a circumnuclear, molecular, and dusty disk forms, as observed in the galactic center. In the high-luminosity regime, large individual dust clouds become unbound due to the strong radiation pressure. The torus should thus consist only of smaller clouds. As a result, the covering factor and apparent scale height decrease with luminosity, so that the fraction of type 1 AGN should be larger at higher luminosities (and high radiative efficiency). This picture is consistent with recent survey number statistics (Fig. 25) and offers a physical explanation for the long-standing phenomenon of "receding tori"; i.e., the increase of the fraction of type 1 AGN with luminosity (see Fig. 25). (see Hönig & Beckert 2007)

4.6 Dynamical models for accretion in a clumpy AGN torus

For the interpretation of high spatial resolution infrared observations of AGN, detailed models of the dusty environment of galactic nuclei on pc-scales are required. We develop consistent dynamical models for clumpy and dusty circumnuclear tori based on a scenario introduced in Beckert & Duschl (2004, A&A 426, 445). A large number of cold, dusty, and self-gravitating clouds form the basis of the model.

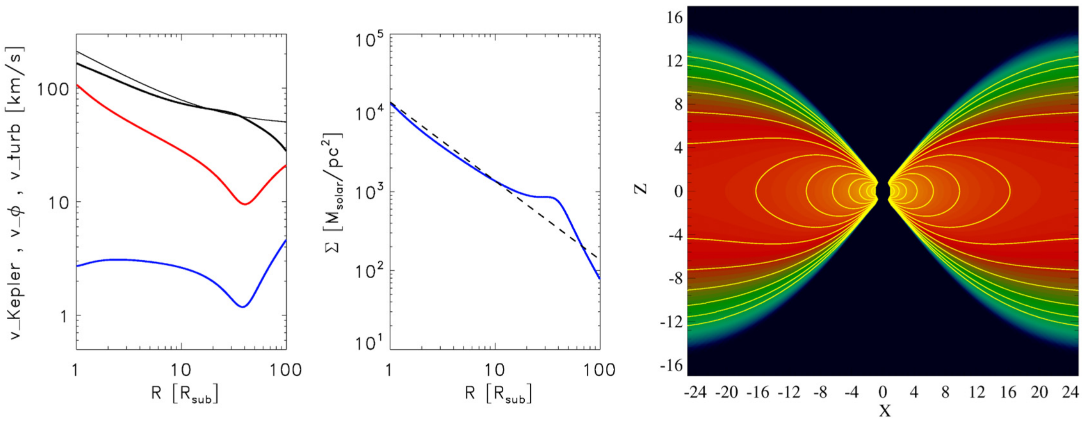

Figure 26 *Results for the structure of our dynamical clumpy torus model. Left: The three characteristic velocities of clouds in the torus as a function of radius (rotation: thick black line; turbulence: red; radial accretion velocity: blue) are compared with the local Keplerian velocity (thin black line). Middle: The surface mass density (thick blue line) shows a strong enhancement above the power-law approximation (dashed line) in the circularization region, where turbulent and radial accretion velocity have their minimum. Right: A meridional cut through the mass density distribution of clouds in the torus shows the increase of scale height with distance from the center and the flattening of the torus near the circularization region at X~30. The spatial scale is in units of the dust sublimation radius. The color scale was chosen to highlight the dense torus mid-plane in red, the low density region in green, and the outflow cavity beyond the cut-off height in dark blue.*

They move on inclined, elliptical orbits in the deep potential well of the galactic nucleus. The clouds experience frequent cloud-cloud collisions due to their large cross sections. During the collisions, the clouds exchange angular momentum and dissipate kinetic energy. The collisions allow a net transport of clouds towards the center, forming an accretion flow. We find stationary models where the gain of kinetic energy in the potential of the nucleus from accretion is balanced by the dissipation in cloud-cloud collisions. In addition, we include the advection of energy and pressure gradients in the momentum equations, which are important for tori with large vertical scale heights. As a result, we find global solutions for the distribution of clouds, the thickness of the torus, and the characteristic velocities of clouds for this clumpy torus model (Fig. 26). For the first time, these models are able to satisfy inner and outer boundary conditions for density and velocities to smoothly connect to the inflow of matter from galactic scales. The torus consists of low density, slowly rotating, and almost freely falling material at large radii, a circularization region with high densities, and a central torus with moderate mass density and thickness (Fig. 26, left). (Beckert, submitted)

4.7 The inner radius of AGN tori and the near-IR brightness of the accretion disk

Direct imaging of and understanding the innermost torus region are key goals in IR interferometry of AGNs since this region is very likely where the actual feeding of the putative accretion disk around a supermassive black hole occurs. We have studied two quantities which are critical for IR interferometry of AGNs: (1) the near-IR brightness of the accretion disk compared to the torus and (2) the inner radius of the torus.

To estimate the flux fraction from the accretion disk, we examined the near-IR colors of unresolved nuclei in the HST/NICMOS images of nearby type 1 AGNs on a color-color diagram through careful 2-D

PSF+host-galaxy decompositions (Fig. 27). Despite the structural and spectral complications of AGN tori, our 3-D clumpy torus modeling and the color-color diagram have demonstrated that the directly-seen inner torus (i.e. seen in type 1 inclinations) essentially has almost a single-temperature blackbody spectrum, with only a minor contribution from the accretion disk. The disk flux fraction is as small as ≤25% at 2.2 μm. This has led us to believe that we will be able to robustly determine the size of the innermost torus using near-IR long-baseline interferometry without complications from the disk.

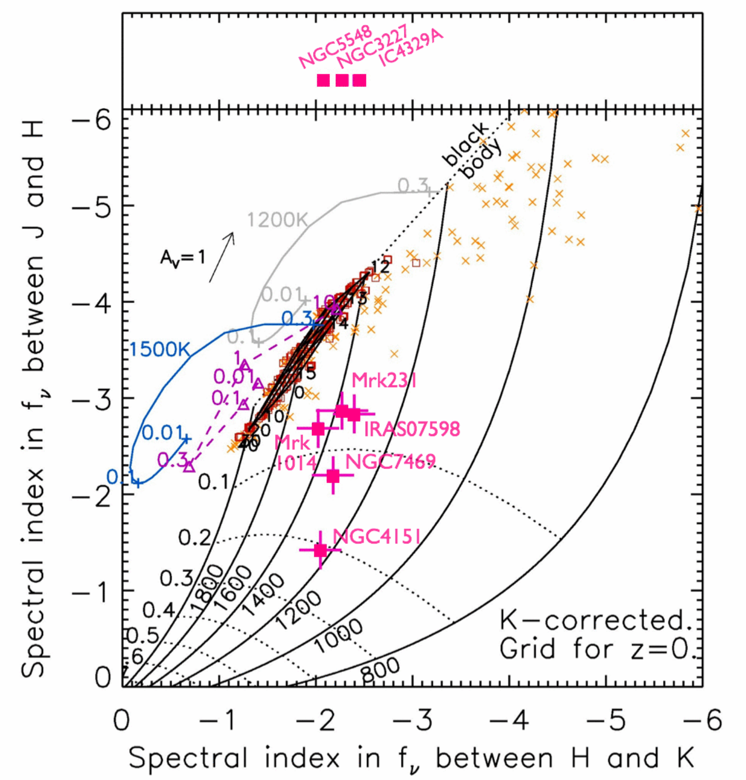

Figure 27 Color-color diagram for the unresolved nuclei in HST/NICMOS images of nearby type 1 AGNs (pink squares with error bars). The large grid represents a blackbody with different temperatures (solid curves, 800-1800 K) plus a blue power-law near-IR tail of an accretion disk with different fractional contributions f_{AD} in the K band (dotted curves; 0, 0.1, 0.2, etc.). The red squares and the overlayed small & flat black grid, labeled with inclinations (0−40°) and temperature (12−15, in units of 100 K), are the colors of our clumpy torus models with type 1 inclinations, while the orange crosses represent type 2s. (Gray and blue lines: optically thin graphite grains for different temperatures in K and grain size in μm; purple line: silicate grains of 1500 K.) The observed colors (pink squares with error bars) suggest a dust sublimation temperature of ≤1500 K and f_{AD} ≤25% (see text).

The inner radius of the torus can be calculated as a dust sublimation radius assuming the standard properties of the interstellar dust grains (Barvainis 1987, ApJ 320, 537). On the other hand, the radius can be probed by measuring the response time of the innermost torus to the variation of the accretion disk which is directly heating up the torus. Surprisingly, we found that this time-lag radius in the literature (Suganuma et al. 2006, ApJ 639, 46) is systematically smaller by a factor of ∼3 than the standard sublimation radius. Based on the constraints on the sublimation temperature given by our HST study above, this discrepancy very likely suggests the dominance of large-size grains in the innermost tori. All these properties can be tested by future VLTI measurements. (Kishimoto et al. 2007, accepted)

5 THEORETICAL STUDIES: ULTRA HIGH ENERGY COSMIC RAYS, NEUTRINOS, GALACTIC COSMIC RAYS, AND DARK MATTER

The sources of ultra high energy cosmic ray particles are not yet identified. We have explored, for some time, the concepts that a) new physics, b) gamma ray bursts, or c) active galactic nuclei could be the sources, and have now prepared further work to identify possible sources, study their physics, and the expected spectrum and sky distribution of arriving events. Our main proposal for the origin of ultra high energy cosmic rays has consistently been that radio galaxies are the sources. AUGER can be expected to resolve this question soon, from the observed spectrum (Fig. 28) and sky distribution. In parallel, we explore the origin of the not yet detected high energy neutrinos. For galactic cosmic rays, we have further explored the concept that the explosions into the magnetic winds of very massive stars produce more energetic cosmic rays, but also study galactic jets emanating from compact stars. Our proposal that dark matter decay can strongly enhance star formation in the very early universe has been verified.

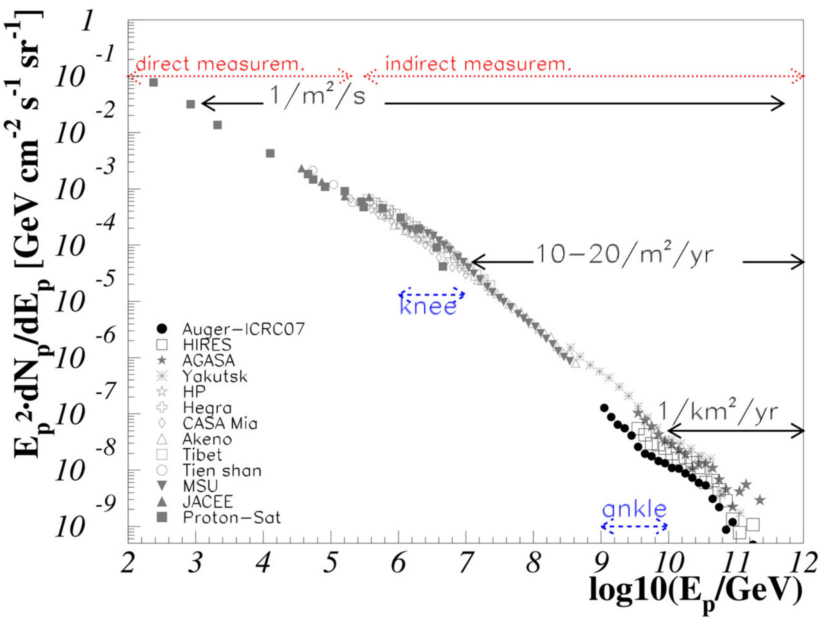

Figure 28 All-particle cosmic ray spectrum from many earlier experiments. Filled circles at the highest energies are recent results from Auger (ICRC 2007), clearly showing the GZK cut-off, due to the interaction with the cosmic microwave background. This is the spectrum which has to be explained.

5.1 Ultra high energy cosmic rays

The origin of the highest energy cosmic rays is one of the oldest quests in fundamental physics, as these particles have an energy more than a million times higher than any existing or planned accelerator on Earth. Radio galaxy hot spots and shocks in jets are prime candidates to produce the highest energy cosmic rays, in relativistic jets emanating from nearly all black holes (Fig. 29). We have defined reliable samples of active sources (Fig. 30), such as black holes and galaxies active in star formation. Using these complete samples, we worked out their individual contribution, modeled their path to us (Fig. 31), and thus have an explanation for the spectrum (Fig. 32). The AUGER array data will decide soon where the highest energy cosmic rays come from, framing the next quests on the origin of very high energy neutrinos (Fig. 33) and perhaps other particles. (see Biermann & Frampton 2006; Apel et al. 2006; Petrovic et al. 2007; Biermann et al. 2007; Abraham, et al. 2007; Buitink et al. 2007; Meli et al. 2007)

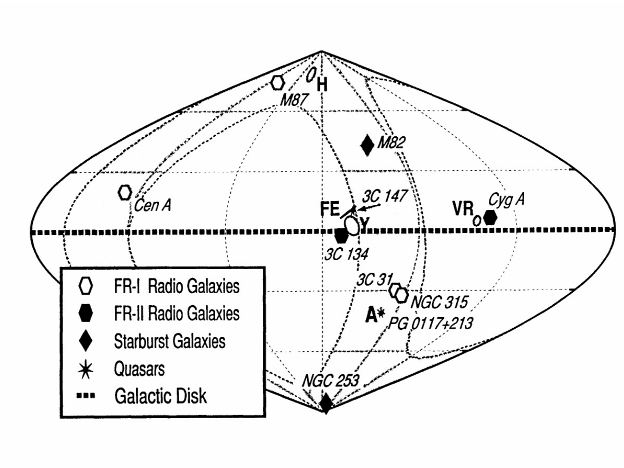

Figure 29 Arrival directions of the most energetic cosmic rays as of 1994, from AGASA (A), Fly's Eye (FE), Haverah Park (H), Volcano Ranch (VR) and Yakutsk (Y), and the location of various outstanding FR-II, FR-I radio galaxies, of some quasars and starburst galaxies, in Galactic coordinates, with the anti-center at the symmetry center. The supergalactic plane is shown shaded. This is our prediction to be compared with the data.

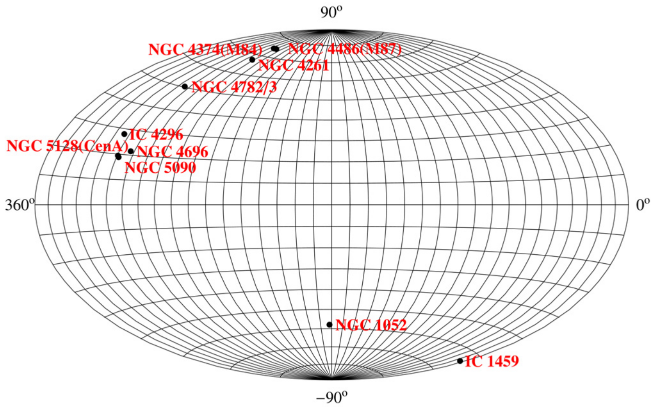

***Figure 30** Sample of the 10 strongest candidate sources for the origin of ultra high energy cosmic rays, selected at 5 GHz and 2 micron, in Galactic coordinates, with the anti-center at the symmetry center. This is our best estimate at present for the strongest contributing sources of ultra high energy cosmic rays.*

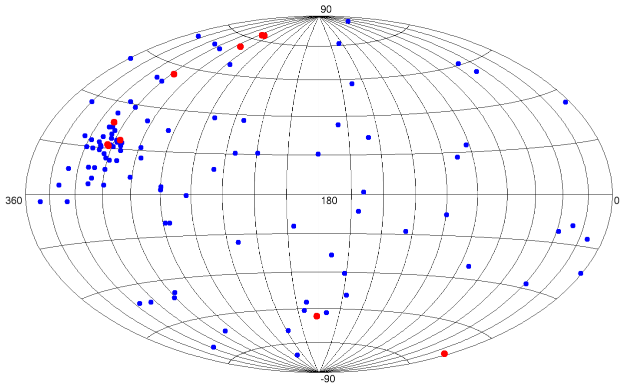

***Figure 31** Current best prediction of the arrival directions of ultra high energy cosmic rays (blue dots), in a powerlaw scattering model, from the strongest ten predicted cosmic ray sources (red dots) in the spin-down approximation for powering the jets and in an Aitoff projection.*

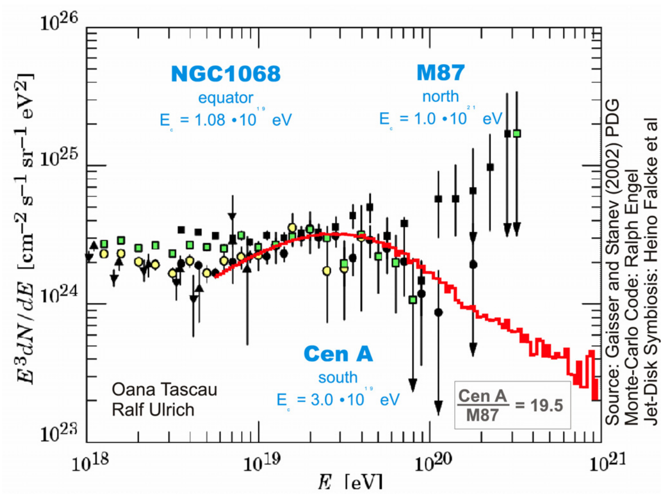

***Figure 32** This spectrum shows our best fit to the data of the spectrum of ultra high energy cosmic rays, including only three sources, NGC1068, Cen A, and M87. The fit was achieved by setting the ratio of the flux of Cen A relative to M87 to about 20. This implies that in the sky distribution of events observed with AUGER, there should be a bunching near Cen A, as the spectral fit requires it to be stronger than any other source.*

5.2 Astrophysical implications of high energy neutrino limits

While the origin of high energy neutrinos is still not certain, the current upper limits to the emission from any class of sources does provide strong limits: Current neutrino detectors are already able to set constraints which are in the range of some emission models. In particular, the Antarctic Muon And Neutrino Detection Array (AMANDA) has presented the most restrictive limit on diffuse neutrino emission so far. We used the limits to constrain the predicted correlation of EGRET-detected diffuse emission and neutrino emission. Also, we constrain the correlation between X-ray and neutrino emission (Fig. 33). We presented further results for source classes like TeV blazars and FR-II galaxies. Starting from the source catalogs examined so-far for the stacking method, we discussed further potential catalogs and examine the possibilities of the second generation neutrino telescopes IceCube and KM3NeT. (see Achterberg et al. 2006; Becker et al. 2007)

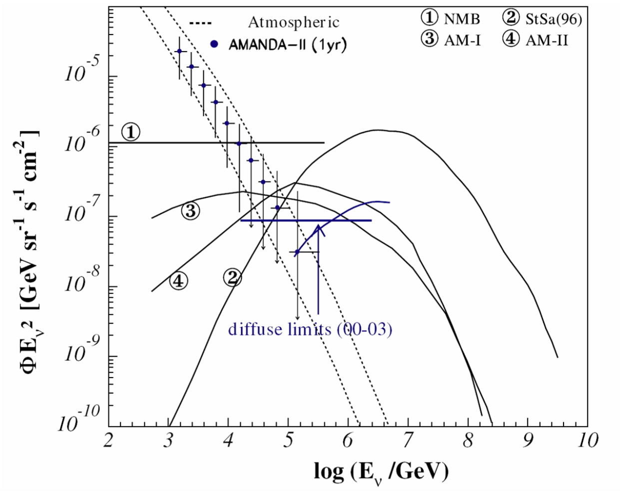

Figure 33 Observed fluxes of atmospheric high energy neutrinos as a function of neutrino energy. The various measurements all match the predicted neutrino flux, derived from cosmic ray interaction in the Earth's atmosphere. We include various models predicting the high energy neutrino flux from Active Galactic Nuclei. All these models have been corrected for neutrino oscillations. We exclude all models in their published form by AMANDA's diffuse limit. The typical E^{-2} limit is represented by the horizontal line.

5.3 Galactic cosmic rays

The origin of Galactic cosmic rays is still not certain, except that we have reached a consensus that the cosmic rays arise from supernova explosions. As we have argued for some time, massive star supernovae explode into their wind, and so the acceleration of cosmic rays starts in the highly enriched wind of the star. We have shown that the interaction near the supernova and its wind bubble is the dominant source of γ-rays, and spallation secondaries seem best suited to explain the EGRET γ-spectrum of the inner Galaxy, the abundances of light elements, the observed anti-protons and the observed positrons. The

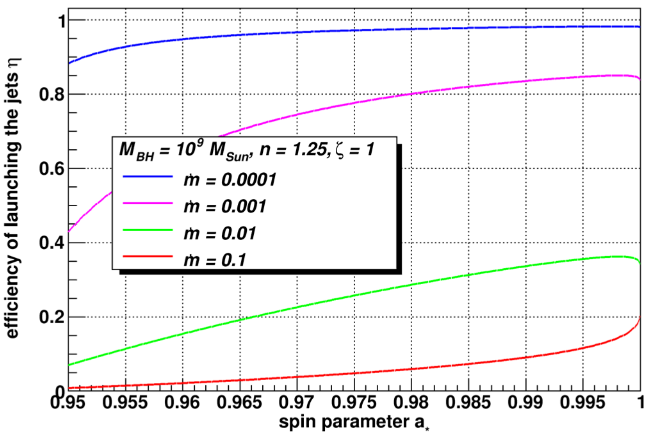

Figure 34 Efficiency of launching a jet from a spinning black hole as a function of the spin parameter for different accretion rates. This is valid for black hole masses on all observed scales.

chemical abundances are best described as resulting from the chemical composition of massive star winds. This implies a supernova mechanism. This mechanism naturally allows us to understand jet-supernovae and gamma ray bursts from its underlying symmetry. Gamma ray bursts are believed to produce black holes. We have made predictions on the efficiency of powering jets (Fig. 34), with data of active black holes on all mass scales, which can now be verified. A key theoretical question remains open: the origin of magnetic fields. (see Biermann 2006; Ikhsanov & Biermann 2006)

5.4 Magnetic field upper limits for jet formation

To test the connection of jets, which accelerate particles, and their host black holes, we study galactic active stars: very strong magnetic fields on the surface of neutron stars (Fig. 35) or in the accretion disk of black holes which inhibit the production of jets. We quantify the magnetic field strength for the jet formation. By using the Alfvén Radius (R_A), we study the basic condition, $R_A/R_* = 1$ or $R_A/R_{LSO} = 1$, (LSO=last stable orbit), in its dependency with the magnetic field strength and the mass accretion rate, and we analyse these results in the case of neutron star and black hole accretor systems respectively. For this purpose, we did a systematic search of all available observational data of the magnetic field strength and the mass accretion rate. The association of a classical X-ray pulsar (i.e. $B \sim 10^{12}$ G) with jets is excluded even if accreting at the Eddington critical rate. Z-sources may develop jets for $B \leq 10^{8.2}$ G whereas Atoll-sources are potential sources for jets if $B \leq 10^{7.7}$ G. It is not ruled out that a millisecond X-ray pulsar could develop jets, at least for those sources where $B \leq 10^{7.5}$ G. In this case, the millisecond X-ray pulsar could switch to a microquasar phase during its maximum accretion rate. For stellar-mass black hole X-ray binaries, the condition is that $B \leq 1.35 \times 10^8$ G and $B \leq 5 \times 10^8$ G at the last stable orbit for a Schwarzschild and a Kerr black hole, respectively. For active galactic nuclei, it reaches $B \leq 10^{5.4-5.9}$ G for each kind of black hole. Most of these general and theoretical results are in complete agreement with observational data. (see Massi & Kaufman-Bernardó 2007)

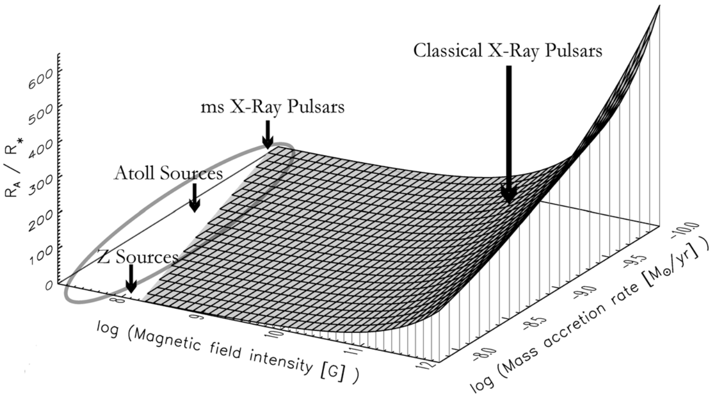

Figure 35 *3-D plot of the Alvén radius normalised to the stellar radius (R_A/R_*). The intersection between the function and the $R_A/R_*=1$ plane indicates the combination of the magnetic field and the mass accretion rate values for which plasma pressure, P_p, and magnetic field pressure, P_B, balance each other at the surface of the star. This ensures that the initial condition for jet formation ($P_B < P_p$) is fulfilled all over the accretion disk.*

5.5 Diffusive acceleration at oblique shocks and the knee in the cosmic ray spectrum

For the origin of cosmic rays and their acceleration in a shock wave region, we need to understand the rate of acceleration. Sampling all directions, i.e. 4π, most shocks are highly oblique in the orientation of the prevailing magnetic field and the shock normal, and in a stellar wind, the magnetic field is highly oblique. We have evaluated the rate of the maximum energy and the acceleration rate that cosmic rays acquire in the non-relativistic diffusive shock acceleration as it could apply during their lifetime in various astrophysical sites, where highly oblique shocks exist. We numerically examine (using Monte-Carlo simulations) the effect of the diffusion coefficients on the energy gain and the acceleration rate by testing the role between the obliquity of the magnetic field to the shock normal and the significance of both perpendicular cross-field diffusion and parallel diffusion coefficients to the acceleration rate. We find and justify previous analytical work that in highly oblique shocks, the smaller the perpendicular diffusion gets compared to the parallel diffusion coefficient values, the greater the energy gain of the cosmic rays to be obtained. We claim then an explanation of the cosmic ray spectrum at high energies, between 10^{15} eV and about 10^{18} eV, as we estimate the upper limit of energy that cosmic rays could gain in plausible astrophysical regimes; we interpret by the scenario of cosmic rays which are injected by three different kind of sources, (a) supernovae which explode into the interstellar medium, (b) Red Supergiants, and (c) Wolf-Rayet stars, where the two latter explode into their pre-supernovae winds. (see Meli & Biermann 2006; Meli et al. 2007)

5.6 Dark matter and cosmology

As we now known for over seventy years now, the universe is filled with dark matter, of which we do not know its physical nature. There are many models for dark matter, and we pursue the notion of warm dark matter, right-handed neutrinos, and particles in the keV mass range. This idea connects well to the galaxy structure and galaxy properties, and implies subtle, interesting modifications in structure formation in the early cosmos; for instance, it implies that galaxy masses have a low mass limit, and such a limit has been detected. We have shown that the decay of a right-handed neutrino changes the ionization structure of the gas and so leads to a modification of the abundance of molecular hydrogen in the early universe, thus allowing catastrophic cooling, which enables star formation from redshift 80. We have undertaken X-ray observations which will either rule out or confirm this idea soon. Our most recent analysis places the mass of the right-handed neutrino in this concept of dark matter at 3 ± 1 keV. (see Biermann & Kusenko 2006; Stasielak et al. 2007)

5.7 Degenerate sterile neutrino dark matter in the cores of galaxies

We study the distribution of fermionic dark matter at the center of galaxies using power law density profiles and show that dark matter becomes degenerate for particle masses of a few keV and for distances less than a few parsec from the center of our galaxy. This is a generalization of the notion of warm dark matter. A compact degenerate core forms after galaxy merging and boosts the growth of supermassive black holes at the center of galaxies (Fig. 36). To explain the galactic center black hole with a mass of 3.5×10^6 $M_\odot$ and a supermassive black hole of 3×10^9 $M_\odot$ at a redshift of 6.41 in a SDSS quasar, we require a degenerate core of mass between 3×10^3 $M_\odot$ and 3.5×10^6 $M_\odot$. This constrains the mass of the dark matter particle between 0.6 keV and 82 keV. We argue that the constrained particle could be the long sought dark matter of the Universe that is interpreted here as a sterile neutrino. (see Munyaneza & Biermann 2006)

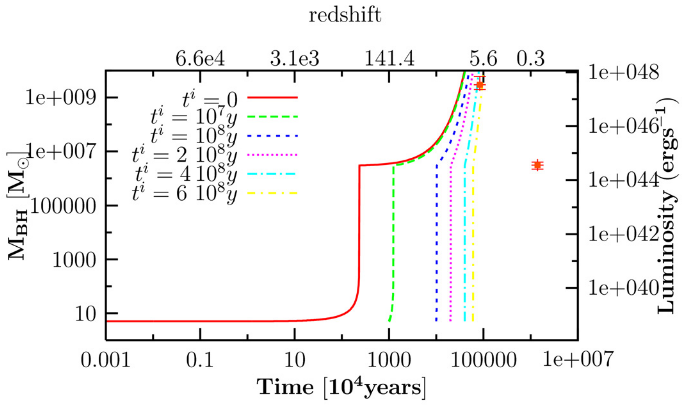

***Figure 36** Growth of a central black hole as a function of time. We give the growth of a seed black hole from dark matter and Eddington-limited baryonic matter accretion, starting with a stellar mass black hole and ending the dark matter accretion with the mass of the Galactic Center black hole.*

People involved: B. Albert, T. Beckert, P.L. Biermann, A. Bogdan, L. Caramete, T. Csengeri, A. Curuţiu, A. Domiziano de Souza, T. Driebe, I. Duţan, S. Ghosh, J. Groh, K.-H. Hofmann, S. Hönig, I. Ileşoi, A. Istrate, M. Kaufman-Bernardó, T. Kellmann, M. Kishimoto, S. Kraus, Z. Kovacs, R. Lachaume, L. Molnar, F. Munyaneza, K. Murakawa, B. Nagy, N. Nardetto, K. Ohnaka, S. Păduroiu, T. Popescu, Th. Preibisch, A. Rosen, D. Schertl, J. Stasielak, A. Streblyanska, F. Tabatabaei, G. Weigelt

Collaborators:
K. Agabi (Univ. Nice), E.J. Ahn (Univ. Delaware), D. Apai (Steward Obs.), P. Antonelli (Obs. de la Côte d'Azur), E. Aristidi (Univ. Nice), C. Baffa (Osservatorio Astrofisico di Arcetri), I. I. Balega, Y.Y. Balega (Special Astrophysical Obs.), J. Becker (Univ. Dortmund), M. Benisty (Univ. Grenoble), J.-P. Berger (Univ. Grenoble), D. Bergman (Rutgers Univ.), H. Beuther (MPIA Heidelberg), G. Bisnovatyi-Kogan (IKI, Moscow), H. Blümer (Univ. Karlsruhe), D. Boboltz (USNO, Washington, DC), A. Boden (CalTech), D. Bosanac (Univ. Zagreb), A.G.A. Brown (Sterrewacht Leiden), S. Casanova (Los Alamos), O. Chesneau (Obs. de la Côte d'Azur, Grasse), A. Chelli (Univ. Grenoble), L. Clavelli (Univ. of Alabama), S. Colafrancesco (ASI-ASDC, ESRIN, Frascati), D. DeMarco (Univ. Delaware), W.J. de Witt (Univ. Grenoble), A. Donea (Monash Univ. Melbourne) J. Dreyer (Univ. Dortmund), W.J. Duschl (Univ. Kiel, Steward Obs.), M. Duget (Obs. de la Côte d'Azur, Grasse), G. Duvert (Univ. Grenoble), M. Elitzur (Univ. Kentucky), R. Engel (Univ. Karlsruhe), T. Enßlin (MPI Astrophysics, Munich), H. Falcke (Univ. of Nijmegen), P. Feautrier (Univ. Grenoble), E. Feigelson (Pennsylvania State Univ.), R. Foy (Centre de Recherche Astronomique de Lyon), D. Fraix-Burnet (Univ. Grenoble), P. Frampton (Univ. NC), C. Galea (Univ. Nijmegen), P. Gandhi (Cambridge Univ.), L. Gergely (Univ. Szeged), L. Glück (Univ. Grenoble), V. Grinin (Pulkovo Obs.), A. Gross (MPI Heidelberg), B. Harms (Univ. Alabama), D. Hasegan (Space Science Institute, Bucharest), G.H. Herbig (Univ. Hawaii), H. Horst (Univ. Kiel), J. Houck (Cornell Univ.), N. Ikhsanov (Univ. Cambridge), P.G. Isar (Univ. Karlsruhe), A. Isella (Osservatorio Astrofisico di Arcetri), K.H. Kampert (Univ. Wuppertal), H. Kang (Pusan Nat. Univ.), A. Kandus (Univ. Ilheus), M. Kiekebusch (ESO), T. Kneiske (Univ. Dortmund), G. Krishna (Tata Inst., Pune), P.P. Kronberg (Univ. Toronto), A. Kusenko (UCLA), S. Lagarde (Obs. de la Côte d'Azur), N. Langer (Univ. Utrecht), E. Le Coarer (Univ. Grenoble), Ch. Leinert (MPIA Heidelberg), F. Lisi (Osservatorio Astrofisico di Arcetri), M. Loewenstein (NASA GSPC), B. Lopez (Obs. de la Côte d'Azur), C.J. Lonsdale (Univ. California) F. Malbet

(Univ. Grenoble), K. Mannheim (Univ. Würzburg), A. Marconi (Osservatorio Astrofisico di Arcetri), I. Mariş (Univ. Karlsruhe), P. Mathias (Obs. de la Côte d'Azur), G. Medina-Tanco (UNAM, Mexico City), A. Meilland (Obs. de la Côte d'Azur), A. Meli (Univ. Athens), S. Mensh'chikov (Inst. for Comput. Astrophysics, Halifax), M. Meyer (Steward Obs.), O. Micu (Univ. Alabama), R. Millan-Gabet (CalTech), F. Millour (Univ. Nice), A.S. Miroshnichenko (Univ. Toledo), S. Moiseenko (IKI, Moscow), J.-L.Monin (Univ. Grenoble), J.D. Monnier (Univ. Michigan), D. Mourard (Obs. de la Côte d'Azur), K. Münich (Univ. Dortmund), B. Nath (RRI, Bangalore), A. Natta (Osservatorio Astrofisico di Arcetri), K.-I. Nishikawa (Univ. Alabama), M. Ostrowski (Jagell. Univ. Cracow), H. Paes (Univ. Alabama), I. Pascucci (Steward Obs.), E. Pedretti (Univ. Michigan), K. Perraut (Univ. Grenoble), C. Perrier (Univ. Grenoble), R. Petrov (Univ. Nice), K. Petrovay (Univ. Budapest), A. Petrusel (Univ. Cluj), M. Polletta (IAP, Paris), A. Popescu (Univ. Bucharest), A.M. Prieto (MPIA, Heidelberg), P. Puget (Univ. Grenoble), G. Pugliese (Univ. Utrecht), Y. Rabbia (Obs. de la Côte d'Azur), W. Rhode (Univ. Dortmund), A. Richichi (ESO), S. Robbe-Dubois (Univ. Nice), R. Roman (Univ. Cluj), G.E. Romero (Univ. La Plata), I. Roussev (Univ. Hawaii), M. Rusu (Univ. Bucharest), D. Ryu (Chungnam Univ., Daejeon), P. Salinari (Osservatorio Astrofisico di Arcetri), A. Sargent (CalTech), F.P. Schloerb (Univ. Massachussets), M. Schöller (ESO), M. Scholz (Univ. Heidelberg), E.S. Seo (Univ. Maryland), A. Smette (ESO), H.E. Smith (Univ. California), M.D. Smith (Armagh Obs.), T. Stanev (Univ. Delaware), P. Stee (Obs. de la Côte d'Azur, Grasse), S. Stoica (IFIN, Bucharest), L.V. Tambovtseva (Pulkovo Obs.), O. Taşcău (Univ. Wuppertal), E. Tatulli (Univ. Grenoble), S. Ter-Antonyan (Univ. Erewan), L. Testi (Osservatorio Astrofisico di Arcetri), G. Thomson (Rutgers Univ.), G. Torres (CfA, Harvard), G. Torricelli- Ciamponi (Acetric Obs.), W.A. Traub (Harvard-Smithsonian Center for Astrophysics), P. Tuthill (Univ. Sydney), R. Ulrich (Univ. Karlsruhe), R. van Boekel (MPIA Heidelberg), M. Vannier (Univ. Nice), A. Vasile (Inst. for Space Science, Bucharest), S. Vidrih (Univ. Ljubljana), B. Vollmer (Univ. Strasbourg), Y. Wang (NAO, CAS, Beijing), P.J. Wiita (Univ. Georgia), D. Weedman (Cornell Univ.), M. Wittkowski (ESO), P.R. Wood (Australian Nat. Univ.), E. Young (Steward Obs.), F. Yuan (Academy of Science, Shanghai), Ch. Zier (Bangalore Univ.), H. Zinnecker (AIP), G. Zins (Univ. Grenoble), T. Zwitter (Univ. Ljubljana)